Journal Pre-proof

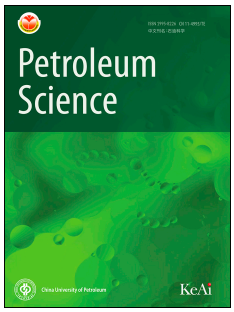

Quantitative effect of kerogen type on the hydrocarbon generation potential of Paleogene lacustrine source rocks, Liaohe Western Depression

Sha-Sha Hui, Xiong-Qi Pang, Fu-Jie Jiang, Chen-Xi Wang, Shu-Xing Mei, Tao Hu, Hong Pang, Min Li, Xiao-Long Zhou, Kan-Yuan Shi

PII: S1995-8226(23)00237-6

DOI: https://doi.org/10.1016/j.petsci.2023.09.004

Reference: PETSCI 620

To appear in: *Petroleum Science*

Received Date: 8 January 2023

Revised Date: 23 June 2023

Accepted Date: 4 September 2023

Please cite this article as: Hui, S.-S., Pang, X.-Q., Jiang, F.-J., Wang, C.-X., Mei, S.-X., Hu, T., Pang, H., Li, M., Zhou, X.-L., Shi, K.-Y., Quantitative effect of kerogen type on the hydrocarbon generation potential of Paleogene lacustrine source rocks, Liaohe Western Depression, *Petroleum Science* (2023), doi: https://doi.org/10.1016/j.petsci.2023.09.004.

Quantitative effect of kerogen type on the hydrocarbon generation potential of Paleogene lacustrine source rocks, Liaohe Western Depression

Sha-Sha Hui [a,b], Xiong-Qi Pang [a,b,*], Fu-Jie Jiang [a,b], Chen-Xi Wang [a,b], Shu-Xing Mei [a,b], Tao Hu [a,b], Hong Pang [a,b], Min Li [a,b], Xiao-Long Zhou [c], Kan-Yuan Shi [a,b,*]

[a] State Key Laboratory of Petroleum Resources and Prospecting, China University of Petroleum, Beijing, 102249, China

[b] College of Geosciences, China University of Petroleum (Beijing), Beijing, 102249, China

[c] Exploration and Development Research Institute, PetroChina Liaohe Oilfield Company, Panjin, Liaoning, 124010, China

*Corresponding authors: E-mail address: pangxq@cup.edu.cn (Xiongqi Pang); shikycup@163.com (Kanyuan Shi)

Abstract: Kerogen types exert a decisive effect on the onset and capacity of hydrocarbon generation of source rocks. Lacustrine source rocks in the Liaohe Western Depression are characterized by thick deposition, high total organic carbon (*TOC*) content, various kerogen types, and a wide range of thermal maturity. Consequently, their hydrocarbon generation potential and resource estimation can be misinterpreted. In this study, geochemical tests, numerical analysis, hydrocarbon generation kinetics, and basin modeling were integrated to investigate the differential effects of kerogen types on the hydrocarbon generation potential of lacustrine source rocks. Optimized hydrocarbon generation and expulsion (HGE) models of different kerogen types were established quantitatively upon abundant Rock-Eval/*TOC*/vitrinite reflectance (*R*o) datasets. Three sets of good–excellent source rocks deposited in the fourth (Es4), third (Es3), and first (Es1) members of Paleogene Shahejie Formation, are predominantly types I–II$_1$, II$_1$–II$_2$, and II–III, respectively. The activation energy of types I–II$_2$ kerogen is concentrated (180~230 kcal/mol), whereas that of type III kerogen is widely

distributed (150~280 kcal/mol). The original hydrocarbon generation potentials of types I, II_1, II_2, and III kerogens are 790, 510, 270, and 85 mg/g *TOC*, respectively. The *R*o values of the hydrocarbon generation threshold for type I–III source rocks gradually increase from 0.42% to 0.74%, and *R*o values of the hydrocarbon expulsion threshold increase from 0.49% to 0.87%. Types I and II_1 source rocks are characterized by earlier hydrocarbon generation, more rapid hydrocarbon expulsion, and narrower hydrocarbon generation windows than types II_2 and III source rocks. The kerogen types also affect the HGE history and resource potential. Three types (conventional, tight, and shale oil/gas) and three levels (realistic, expected, and prospective) of hydrocarbon resources of different members in the Liaohe Western Depression are evaluated. Findings suggest that the Es3 member has considerable conventional and unconventional hydrocarbon resources. This study can quantitatively characterize the hydrocarbon generation potential of source rocks with different kerogen types, and facilitate a quick and accurate assessment of hydrocarbon resources, providing strategies for future oil and gas exploration.

Keywords: Kerogen type; Hydrocarbon generation potential; Lacustrine source rocks; Liaohe Western Depression.

1. Introduction

Against the background of global increase in demand for resources and the limited energy supply, unconventional hydrocarbon resources are accorded wide-ranging emphasis in the international energy market (Jarvie et al., 2007; Zou et al., 2018; Hu et al., 2022a, b; Shi et al., 2022; Wang et al., 2022;). Paleogene lacustrine shales in the Bohai Bay Basin, serving as high-quality source rocks, have provided a sufficient hydrocarbon supply for conventional reservoirs and have emerged as the primary focus of shale oil exploration in recent years (Zou et al., 2019; Zhao et al., 2020; Li et al.,

2022). However, lacustrine source rocks exhibit rapid changes in sedimentary facies, lithology, and source inputs, corresponding to great variations in the scale and thickness of source rocks, especially in kerogen types, which results in the inaccurate assessment of resource potential (Katz and Lin, 2014; Hu et al., 2021; Yang et al., 2022; Zhu et al., 2022). Lacustrine organic-rich shales with excellent quality but different kerogen types have considerably varying hydrocarbon generation and expulsion (HGE) characteristics (Chen et al., 2015). Therefore, studying the influence of different kerogen types on the hydrocarbon generation potential of lacustrine source rocks is conducive to resource potential assessment.

Considering the strong heterogeneity of lacustrine source rocks, a reliable and cost-effective method is required to quantify the HGE capacities of these source rocks with different kerogen types. Hydrocarbon generation kinetics and thermal simulation experiments are effective methods for investigating the HGE characteristics (Behar et al., 1992; Wei et al., 2012; Ma et al., 2017; Zhang et al., 2020; He et al., 2021; Chen et al., 2022; Yang et al., 2022). However, due to the complex chemical structure of kerogen, the hydrocarbon generation kinetics can vary greatly even for the same kerogen type, leading to great differences in hydrocarbon generation history (Tegelaar and Noble, 1994; Wang et al., 2011; Chen et al., 2019). Similarly, considering the heterogeneity of shale samples and the high experimental cost, the application of thermal simulation results to restore the HGE history under complex geological conditions must be considered carefully. Recently, Rock-Eval analysis has been widely used to study kerogen kinetics, providing a quick and effective evaluation method for source rocks (Bordenave et al., 1993; Chen et al., 2021). Based on the abundant and easily available Rock-Eval data, the hydrocarbon generation potential method was proposed to establish the HGE model of source rocks and quantitatively calculate the

HGE amount (Pang et al., 2005). Additionally, in combination with the concept of dynamic fields, different types of hydrocarbon resources can be distinguished (Pang et al., 2020, 2021, 2022).

Previous studies have optimized the hydrocarbon generation potential method, such as restoring the original total organic carbon (*TOC*) content (Peng et al., 2016; Zheng et al., 2019), calculating the evaporation loss of light hydrocarbons (Chen et al., 2018; Wang et al., 2020), and correcting the maximum hydrocarbon generation curve (Li et al., 2020). Nevertheless, the influence of different kerogen types on the HGE model has rarely been studied, which also affects the HGE thresholds (Snowdon, 1991; Petersen et al., 2010; Chen et al., 2015; Zhu et al., 2022). Additionally, the variation in the Rock-Eval/*TOC* datasets and vitrinite reflectance (*R*o) during the complete thermal evolution has not been considered in previous studies, which may lead to the miscalculation of original and residual hydrocarbon generation potential in the immature and mature/overmature stage.

In the Liaohe Western Depression, which is characterized by multicycle sedimentary evolution and unbalanced tectonic movement, three hydrocarbon-generating sags were successively formed from north to south, and three sets of large-scale and high-quality lacustrine source rocks were developed (Hui et al., 2022; **Fig. 1**). The diverse kerogen types and wide distribution range of thermal maturity are favorable for studying the differential evolution of source rocks. This study aims to establish the HGE model of Paleogene lacustrine source rocks in the Liaohe Western Depression under the complete maturity sequence using an optimized method and to investigate the differential influence of kerogen types on HGE capacities. Combined with the results of hydrocarbon generation kinetics and basin modeling, the HGE process of lacustrine source rocks in the Liaohe Western Depression will be reconstructed. A more practical

motivation is to improve the evaluation accuracy of conventional and unconventional hydrocarbon resources and assist oilfield in formulating better development strategies.

Fig. 1. Regional map showing the location (a), structure subdivision (b), and geological profile (c) of the Liaohe Western Depression, Bohai Bay Basin.

2. Geological setting

The Liaohe Western Depression is the largest oil-generating depression in the Liaohe Basin, covering an area of ~2530 km^2 (**Fig. 1**). It is a Mesozoic–Cenozoic rift depression, and includes nine secondary tectonic units (Zhang et al., 2013). The strata of the Paleogene Shahejie Formation (Es) includes Es4, Es3, Es2, and Es1 members from bottom to top (**Fig. 2**). Large-scale and high-quality source rocks were deposited in the Es4, Es3, and Es1 members, which provide sufficient hydrocarbon sources for the study area. The differential tectonic evolution resulted in a complex structure framework in the study area (Tong et al., 2008). During the deposition of the Es4 member, the Niuxintuo-Tai'an sag in the north was the sedimentary center, where thick oil shale and dark mudstone developed with a maximum thickness of 700 m (**Fig. 3**). During the deposition of the Es3 member, the Qingshui sag in the south and Chenjia sag in the middle were the sedimentary centers, where thick dark mudstone developed with a maximum thickness of 1800 and 1200 m, respectively. During the deposition of the Es1 member, the southern part of the depression developed a saline semideep lake environment, and the thickness of dark mudstone in the Qingshui sag could reach 600 m (Hui et al., 2022).

Fig. 2. Comprehensive stratigraphic column showing the stratigraphy, depositional environment, and structure evolution of the Liaohe Western Depression.

Fig. 3. Thickness and kerogen type of Shahejie source rocks in the Liaohe Western Depression (modified fromHui et al., 2022).

3. Materials and methods

3.1. Samples and experiments

The dataset was collected from 70 wells in the Liaohe Western Depression, including 645 sets of TOC and Rock-Eval data, 550 sets of R_o data, 270 sets of maceral composition, 9 groups of kerogen kinetics, and 7 groups of hydrocarbon pyrolysis experiments. Most of the datasets were provided by PetroChina Liaohe Oilfield Company.

3.1.1 *TOC* and Rock-Eval pyrolysis

First, diluted hydrochloric acid was used to remove the inorganic carbon in the sample under laboratory conditions. The *TOC* was fully converted into carbon dioxide by high-temperature oxygen flow combustion and then detected using a LECO CSe400 analyzer to obtain the *TOC* content (GB/T 19145-2003). The Rock-Eval pyrolysis experiment was conducted on the Rock-Eval II instrument (GB/T 18602-2012). The sample was heated to 300℃ and 600℃ by hydrogen flow to obtain the amount of free hydrocarbon (S_1) and pyrolysis hydrocarbon (S_2), respectively. To ensure the effectiveness of S_1 and S_2, the maximum temperature (T_{max}) was maintained between 420℃ and 500℃ (Peters, 1986; Riediger et al., 2004).

3.1.2 Determination of vitrinite reflectance

Vitrinite reflectance (*R*o) was measured using a Leica DM4500P polarizing microscope on highly polished rock samples under oil immersion conditions (according to Chinese Petroleum Industry Standard: SY/T 5124-1995). The measured objects are

unstructured homogeneous vitrinite and matrix vitrinite, avoiding the interference of high-reflectivity substances such as pyrite. The measuring points were distributed as evenly as possible and were not less than 30 points for each sample. A standard sample was recalibrated after 2 h.

3.1.3 Organic petrographic analysis

The samples were crushed to 0.5–1 mm. Approximately 5 g of the sample and epoxy resin were placed in a cylindrical mold (diameter of 20–40 mm) at a ratio of 1:1 and stirred evenly. After curing, the epoxy resin was added to a height of ~12 mm. After standing for 24 h, the light sheet was taken out. The maceral observation was performed using a Leica microscope (DM6 M LIBS) in reflected and transmitted light (according to Chinese Petroleum Industry Standard: SY/T 6414-1999). The macerals were quantified by applying the point counting method, and the total effective points of each sample were maintained at no less than 800. The macerals identified in the source rock samples in the study area mainly included sapropelic amorphous, alginite, sapropelic debris, *sporopollenin*, structural vitrinite, unstructured vitrinite, and inertinite.

3.1.4 Hydrocarbon generation kinetics in an open system

The chemical kinetics model adopts the parallel first-order chemical reaction model (Braun and Burnham, 1987). During thermal evolution, the transformation of kerogen is described as a set of independent chemical processes. The reaction rate can be expressed as Eq. (1):

$$\frac{dx}{dt} = -k(T)\mathrm{f}(x) \tag{1}$$

where x represents the fraction of unreacted components; t represents the time; T represents the absolute temperature of the reaction; $k(T)$ is the reaction rate constant; f(x) is a function of reacted mass.

The dependence of $k(T)$ on temperature can be obtained by the Arrhenius equation, as shown in Eq. (2).

$$k(T) = A \cdot \exp(-\frac{E}{RT}) \quad (2)$$

where A represents the pre-exponential or frequency factor; E represents the activation energy; R represents the gas constant.

3.2. Methods

Upon abundant Rock-Eval/*TOC* datasets of natural samples with different maturity, the variations of hydrogen index (*HI*) with thermal maturity index (T_{max} or *R*o) were analyzed to characterize the hydrocarbon generation potential. This is a data-driven approach supported by real data, as shown in Eq. (3) (Chen and Jiang, 2015; Li et al., 2020; Hui et al., 2023; **Fig. 4a**).

$$HI = HI_o \cdot (1 - \exp(-(\frac{R_o}{\beta_1})^{\theta_1})) + c_1 \quad (3)$$

where $HI = (S_2/TOC) \times 100$, mg/g *TOC*; HI_o is the original *HI*, mg/g *TOC*; β_1 and θ_1 are the parameters related to hydrocarbon generation kinetics, which depends on the shape of the fitting curve; c_1 is a constant; and $c_1 = 0$ when the source rocks are immature.

By fitting the relationship between *HI* and T_{max} under a complete maturity sequence, optimal HI_o, β_1, θ_1, and c_1 can be obtained to restore the hydrocarbon generation history. However, the real hydrocarbon generation potential (P_g) should include three parts: the expelled hydrocarbons (Q_e), the generated but retained hydrocarbons (S_1), and the kerogen or residual organic matter (OM) (corresponding to S_2), as shown in Eq. (4).

$$P_g = S_1 + S_2 + Q_e \quad (4)$$

The hydrocarbon generation potential index (*GPI*) is defined as $(S_1 + S_2)/ TOC \times 100$ and represents the hydrocarbon generation capacity of unit OM including the

198 generated hydrocarbons and hydrocarbons that could be generated (Pang et al., 2005).
199 The immature source rock has not yet generated hydrocarbons, and no free hydrocarbon
200 (S_1) is present in the pore. Therefore, the original *GPI* (GPI_o) is equal to the original *HI*
201 (HI_o), as shown in Eq. (5).

202 $$GPI_o = HI_o \tag{5}$$

203 The T_{max} value is easily affected by the S_2 value. Thus, the relationship between
204 *GPI* and the thermal maturity index *R*o was fitted using Origin software and numerical
205 analysis to characterize the variations of hydrocarbon generation potential in this study
206 (**Fig. 4b**), as shown in Eq. (6).

207 $$GPI = GPI_o \cdot (1 - \exp(-(\frac{R_o}{\beta_2})^{\theta_2})) + c_2 \tag{6}$$

208 During the thermal evolution process, kerogen is gradually transformed into
209 hydrocarbons as thermal maturity increases. The extent to which kerogen is converted
210 to hydrocarbons is known as the transformation ratio (T_R) and can be expressed as the
211 ratio between the generated hydrocarbons and the total hydrocarbon generation
212 potential, as shown in Eq. (7) (Justwan and Dahl, 2005; **Fig. 4c**). T_R depends on the
213 quality, type, and maturity of source rocks.

214 $$T_R = \frac{S_1 + Q_e}{S_1 + S_2 + Q_e} = \frac{1200}{HI_o} \cdot \frac{HI_o - HI}{1200 - HI} \tag{7}$$

215 With the increase in maturity, the generated hydrocarbons meet various retention
216 requirements in the pores and begin to discharge as free phase, and the corresponding
217 maturity or depth is called the hydrocarbon expulsion threshold (HET) (Pang et al.,
218 2005). Similarly, the extent to which hydrocarbons are expelled from source rocks is
219 defined as the expulsion ratio (E_R). It represents the proportion of expelled
220 hydrocarbons to the maximum generated hydrocarbon (**Fig. 4c**), as shown in Eq. (8).

$$E_R = \frac{Q_e}{S_1 + S_2 + Q_e} = \frac{1200}{GPI_o} \cdot \frac{GPI_o - GPI}{1200 - GPI} \quad (8)$$

The hydrocarbon expulsion efficiency (f) represents the proportion of expelled hydrocarbons to generated hydrocarbons, as shown in Eq. (9).

$$f = \frac{Q_e}{S_1 + Q_e} = \frac{GPI_o - GPI}{HI_o - HI} \quad (9)$$

Additionally, the rock quality and organic carbon abundance of the source rock will decrease during thermal evolution, which is why the original *TOC* (TOC_o) should be restored (Justwan and Dahl, 2005; Modica and Lapierre, 2012; Chen and Jiang, 2016). In this study, the TOC_o is recovered by establishing the relationship between organic carbon loss and T_R, f, and *TOC*, as shown in Eq. (10) (for the derivation, see Chen and Jiang, 2016). The recovery coefficient (K) represents the proportion of TOC_o to the measured *TOC* and can be obtained by Eq. (11).

$$TOC_o = \frac{TOC}{1 - \alpha \cdot f \cdot T_R \cdot (1 - 1.2 \cdot \frac{TOC}{100})} \quad (10)$$

$$K = \frac{TOC_o}{TOC} \quad (11)$$

where the units of TOC_o and *TOC* are in % and α is related to kerogen type and represents the proportion of effective carbon to total carbon in the sample ($\alpha = HI_o/1200$).

As thermal maturity increases, the source rock starts to generate hydrocarbons, which means that the hydrocarbon generation threshold (HGT) has been reached, corresponding to the decrease of the *HI* value in the HGE model (**Fig. 4b**). With the continuous increase in maturity, hydrocarbons begin to discharge when they reach the HET, and the *GPI* value begins to decrease in the model, which is regarded as the residual GPI (GPI_r).

The hydrocarbon expulsion capacity (q_e) is determined by the GPI_o and GPI_r, as

244 shown in Eq. (12). The maximum hydrocarbon generation capacity (q_g) is the amount
245 of hydrocarbons that could be generated by unit *TOC*, which is equal to GPI_o.

246 $$q_e = GPI_o - GPI_r \quad (12)$$

247 $$q_g = GPI_o \quad (13)$$

248 The hydrocarbon expulsion rate (r_e) is expressed as the variations of *GPI* per 0.1%
249 *R*o interval (**Fig. 4d**). Similarly, the hydrocarbon generation rate (r_g) represents the
250 variations of HI per 0.1% *R*o interval.

251 $$r_e = \frac{d(GPI)}{dR_o} \quad (14)$$

252 $$r_g = \frac{d(HI)}{dR_o} \quad (15)$$

253 Thus far, the HGE model of source rocks has been quantitatively established. The
254 HGE characteristics of source rocks with different kerogen types are obviously different,
255 as shown in the differences in their GPI_o and the thresholds, capacity, and rates of HGE
256 in the model. Combined with the thickness, *TOC* content, and density of source rocks,
257 the HGE intensities (I_g and I_e) can be calculated using Eqs. (16) and (17). The HGE
258 amounts (Q_g and Q_e) can be obtained by integrating the HGE intensities over the whole
259 area of the source rock, as shown in Eqs. (18) and (19). The residual hydrocarbon
260 amount (Q_r) can be obtained using Eq. (20).

261 $$I_g = \int_{R_o} 10^{-3} \cdot q_g \cdot H \cdot \rho \cdot TOC_o \cdot d(R_o) \quad (16)$$

262 $$I_e = \int_{R_o} 10^{-3} \cdot q_e \cdot H \cdot \rho \cdot TOC_o \cdot d(R_o) \quad (17)$$

263 $$Q_g = \int_S \int_{R_o} 10^{-13} \cdot q_g \cdot H \cdot \rho \cdot TOC \cdot d(R_o) d(S) \quad (18)$$

264 $$Q_e = \int_S \int_{R_o} 10^{-13} \cdot q_e \cdot H \cdot \rho \cdot TOC \cdot d(R_o) d(S) \quad (19)$$

$$Q_r = Q_g - Q_e \quad (20)$$

where q_g and q_e are expressed in mg/g *TOC*; I_g and I_e are expressed in 10^4 t/km^2; Q_g, Q_e, and Q_r are expressed in 10^8 t; *H*, *S*, and ρ are the thickness, area, and density of source rocks, expressed in m, m^2, and g/cm^3, respectively; *TOC* and R_o are expressed in %.

Fig. 4. Conceptual hydrocarbon generation and expulsion (HGE) model of source rocks. (a) Variation of *HI* and T_{max} showing the hydrocarbon generation potential. (b) Optimized regression model showing the relationship between *R*o, *HI*, and *GPI*. (c) Variation of T_R and E_R with increasing *R*o showing the degree of HGE. (d) Variation of r_g and r_e with increasing *R*o showing the rate of HGE.

4. Results

4.1. OM abundance

The *TOC* of the Es4 source rock in the Liaohe Western Depression varies greatly, ranging from 0.35% to 12.4% (average of 3.74%) (**Fig. 5a**). The $S_1 + S_2$ value accounts for 0.25–79 mg/g (average of 19 mg/g). According to the evaluation criteria for continental source rocks (Huang et al., 1984; Peters, 1986), the Es4 source rock is a good-to-excellent source rock (**Fig. 5b**). The *TOC* of the Es3 source rock accounts for 0.35%–6.82% (average of 1.85%) (**Fig. 5a**), and its $S_1 + S_2$ value accounts for 0.28%–89.2% (average of 5.4%), indicating that it is a good source rock (**Fig. 5c**). The *TOC* of the Es1 source rock accounts for 0.21%–5.05% (average of 1.8%) (**Fig. 5a**), and the $S_1 + S_2$ value accounts for 0.28%–39.8% (average of 5.1%), showing that it is a good source rock (**Fig. 5d**).

Fig. 5. Source rock potential of the Es4, Es3, and Es1 members in the Liaohe Western

289 Depression. (a) *TOC* box plot. (b–d) (S_1 + S_2) versus *TOC* plot.

290 4.2. OM type

291 The variation between *HI* and T_{max} can be used to classify the kerogen types
292 (Espitalie et al., 1984). As illustrated in **Fig. 6**, the OM types of Shahejie lacustrine
293 source rocks in the Liaohe Western Depression are diverse. The kerogen types of the
294 Es4, Es3, and Es1 source rock are mainly types I–II_1 (~67%), II_1–II_2 (~90%), and II–
295 III (~98%), respectively.

296 **Fig. 7** exhibits the macerals of the Paleogene Shahejie lacustrine source rocks. In
297 the Es4 member, the sapropelic group is the dominant maceral, including amorphous
298 bodies and alginate, containing a small amount of exinite. The Es3 and Es1 source rocks
299 have relatively complex macerals, mainly sapropelic group, followed by vitrinite and
300 inertinite. From the Es4 to Es1 members, the exinite content decreases, whereas the
301 vitrinite and inertinite contents increase.

302

303 **Fig. 6**. Diagram of *HI* vs. T_{max} indicating the OM types of the Shahejie lacustrine source
304 rocks.

305

306 **Fig. 7**. Diagram showing the macerals of the Shahejie lacustrine source rocks.

307 4.3 Organic petrographic

308 The micrographs of the Shahejie lacustrine shale and mudstone samples under
309 transmitted, reflected, and fluorescent light show the development of a well-laminated
310 texture (**Fig. 8**). Dark argillaceous/organic laminae are interbedded with bright
311 carbonate laminae, including dark bioclasts (**Fig. 8a and 8b**). The organic-rich dark
312 laminae formed by the degradation of algae show an obvious brownish-yellow color

313 under fluorescent light. Nonstructured vitrinite is common in the Es3 sample (**Fig. 8c**).
314 The sapropelic group of the Es1 sample is mainly composed of amorphous bodies,
315 mixed with argillaceous materials to form dark lamina (**Fig. 8d**). The laminated texture
316 is widely developed in the source rocks of the Liaohe Western Depression, which is
317 favorable for hydrocarbon generation.
318
319 **Fig. 8**. Optical micrographs showing the organic petrological features of source rocks.
320 (a) Laminated texture, organic-rich grayish–brown oil shale from Well G8 (1435.8 m)
321 in the Es4 member under transmitted, reflected, and fluorescent light. (b) Laminated
322 texture, algae-rich dark-gray mudstone from Well Shuang 202 (4641.9 m) in the Es3
323 member under transmitted, reflected, and fluorescent light. (c) Nonstructured vitrinite,
324 dark-gray calcareous mudstone from Well Shu 74 (1034.6 m) in the Es3 member under
325 transmitted, reflected, and fluorescent light. (d) Laminated texture, brown–gray
326 calcareous shale from Well M31 (2172.7 m) in the Es1+2 member under transmitted,
327 reflected, and fluorescent light.

328 ## 4.4 Thermal maturity

329 T_{max} and *R*o are widely used as indexes of thermal maturity (Tissot and Welte,
330 1984). From the Es4 to Es1 source rocks, the T_{max} values are 422℃–456℃, 421℃–
331 478℃, and 417℃–468℃, with averages of 436℃, 438℃, and 432℃, respectively (**Fig.**
332 **9a–9c**). The *R*o values are mainly 0.21%–0.84%, 0.30%–1.56%, and 0.24%–0.99%,
333 with averages of 0.46%, 0.58%, and 0.49%, respectively (**Fig. 9d–9f**). Results indicate
334 that the Es4 and Es1 source rocks are low maturity to mature, while the thermal maturity
335 of the Es3 source rock varies greatly from low maturity to high maturity.
336
337 **Fig. 9**. Diagram of T_{max} versus depth and *R*o versus depth showing the thermal maturity.

(a–c) T_{max} versus burial depth. (d–f) *R*o versus burial depth.

4.5 Hydrocarbon generation kinetics of different kerogen type

The activation energy (*E*) and frequency factor (*A*) are related to the nature of kerogen and can reflect the capacity of hydrocarbon transformation, which are obtained by the hydrocarbon generation kinetics experiments combined with the KINETICS software (Peters et al., 2015; Chen and Jiang, 2016). To minimize the influence of lithology, mudstone samples with different kerogen types from the Liaohe Western Depression were collected to compare their differences in hydrocarbon generation kinetics, except for the type I oil shale sample of well D16 (**Fig. 10**). The *E* distribution of types I and II_1 kerogen is concentrated in 180~200 kcal/mol (**Fig. 10a–10e**). The dominant *E* of type II_2 kerogen is significantly larger than type I kerogen, ranging from 220 to 240 kcal/mol (**Fig. 10f–10g**). The type III kerogen has a dispersed *E* distribution, ranging from 150 to 280 kcal/mol, indicating that it has a complex chemical structure (**Fig. 10h–i**). The lower *E* of types I and II_1 kerogen indicates that they are more likely to generate hydrocarbons. A detail that must be noticed is that due to the complex molecular structures of kerogen, hydrocarbon generation kinetics experiments on limited source rocks may result in differences in the kinetics properties even for the same kerogen type (Tegelaar and Noble, 1994; Chen and Jiang, 2015). Therefore, it is necessary to characterize the hydrocarbon generation capacities of source rocks by using abundant Rock-Eval/*TOC*/*R*o datasets.

Fig. 10. Distribution characteristics of the activation energy of different kerogen types in the Liaohe Western Depression. (a, b) Type I kerogen. (c–e) Type II_1 kerogen. (f, g) Type II_2 kerogen. (h, i) Type III kerogen.

4.6 Optimal fitted HGE model of different OM-type source rocks

Considering the constraints of kerogen types and the thermal maturity of Paleogene lacustrine source rocks, abundant Rock-Eval/*TOC*/*R*o datasets of source rocks with different kerogen types from immature to the mature stage were collected from PetroChina Liaohe Oilfield Company to improve the reliability of the HGE model. The pyrolysis experiment results were supplemented to indicate the variation of the HGE process of source rocks from the mature to overmature stage, and the HGE models under complete maturity sequence were established. The details of the pyrolysis experiment are reported in a previous study (Hui et al., 2023). When the Rock-Eval/*TOC*/*R*o datasets are composed of abundant samples with the same kerogen type but different thermal maturity, the datasets need to be calibrated to ensure that they conform to similar maturation paths. As shown in **Fig. 11**, the fitted HI curves show good fitting relationships with measured *HI* as R_o increases. The HI_o of types I, II_1, II_2, and III source rocks are 790, 510, 270, and 85 mg/g TOC, respectively, indicating that the hydrocarbon potential was gradually depleted (Chen et al., 2014; Zhu et al., 2022; **Fig. 11a, 11c, 11e, and 11g**). From type I to III source rocks, the β_1 of the four fitted curves are 0.64, 0.68, 0.87, and 1.20, respectively, indicating the maturity of the four types of source rocks corresponding to a large amount of hydrocarbon generation. The residuals of the regression models of different types of source rocks represent the difference between the measured *HI* and the fitted *HI*, which are evenly and symmetrically distributed on both sides of 0, indicating that the models are unbiased (**Fig. 11b, 11d, 11f, and 11h**). Similarly, the fitted *GPI* curves exhibit good correlations with the measured *GPI*, with R^2 ranging from 0.81 to 0.91 (**Fig. 12**). The GPI_o of different types of kerogen is equal to HI_o. The residual distribution of type I source rock is slightly asymmetric, whereas that of the other source rocks is relatively uniform. The

optimal parameters in GPI and HI regression models are illustrated in **Figs. 11 and 12**.

Fig. 11. Regression models of HI versus R_o fitted by the Rock-Eval datasets of different kerogen types and their corresponding residual distribution.

Fig. 12. Regression models of *GPI* versus *R*o fitted by the Rock-Eval datasets of different kerogen types and their corresponding residual distribution.

5. Discussion

5.1. Control of kerogen type on HGE pattern

Upon the optimal regression models of *GPI* and *HI*, the HGE models of types I–III source rocks were established quantitatively by numerical analysis and compared with the geological conditions (**Fig. 13**). The GPI_o of types I–III source rocks gradually decreases (Chen et al., 2014; Zhu et al., 2022), which fit the fact that the capacity of hydrocarbon generation decreases from type I to III source rocks. The HGT and HET of different types of source rocks vary significantly. The HGTs of types I, II_1, II_2, and III source rocks are 0.42% *R*o, 0.50% *R*o, 0.62% *R*o, and 0.74% *R*o, respectively. The HETs of types I, II_1, II_2, and III source rocks are 0.49% *R*o, 0.56% *R*o, 0.69% *R*o, and 0.87% *R*o, respectively. The increasing HGT and HET of the four types of source rocks indicate the increasing difficulty for source rocks to generate and expel hydrocarbons (Tegelaar and Noble, 1994; Chen et al., 2015), which is comparable to the results of the hydrocarbon generation kinetics (**Fig. 10**). Types I and II_1 kerogens have a narrower *E* distribution and a lower average *E* than types II_2 and III kerogens, thereby verifying their early onset of hydrocarbon generation and narrow hydrocarbon generation window. This conclusion also provides theoretical support for the exploration of low-

411 maturity oil in the Es4 member in the northern part of the study area.

412 As the maturity increases, types I and II_1 source rocks begin to generate and
413 discharge hydrocarbons rapidly after reaching the HGT and HET. Their T_R and E_R
414 increase rapidly, while the r_g and r_e increase rapidly and then decrease rapidly (**Fig.**
415 **14a–14d**). In contrast, the T_R, E_R, r_g, and r_e of type II_2 source rocks are obviously slower
416 and lower than types I and II_1 source rocks. The OM of type III kerogen mainly comes
417 from terrestrial higher plants; its T_R, E_R, r_g, and r_e are obviously different from types I–
418 III source rocks. Although the HGT and HET of type III source rock are relatively
419 backward, it has considerable gas generation potential, which is mainly due to its unique
420 hydrocarbon generation mechanism, namely, defunctionalization (Ungerer, 1990;
421 Zhang et al., 2020). The T_R, E_R, r_g, and r_e of Paleogene lacustrine source rocks vary
422 with kerogen type and thermal maturity, which lead to the complicated distribution of
423 hydrocarbon resources in the Liaohe Western Depression.

424

425 **Fig. 13**. Optimized HGE models of types I–III source rocks in the Liaohe Western
426 Depression.

427

428 **Fig. 14**. Variation of (a) transformation ratio (T_R), (b) expulsion ratio (E_R), (c)
429 hydrocarbon generation rate (r_g), and (d) hydrocarbon expulsion rate (r_e) with
430 increasing thermal maturity of types I–III source rocks.

431 5.2. Construction of the HGE history of Shahejie source rocks

432 In previous studies, source rocks were considered to generate hydrocarbons when
433 they reach a certain depth or maturity despite their kerogen types (Guo et al., 2012,
434 2013). Based on two-dimensional basin modeling, the HGE history of two wells
435 (Shu123 and SS3) is restored considering the source rock types in each member (**Fig.**

436 **15**). For Shu123, the Es4 source rock is mainly type I kerogen, which reached the HGT
437 (*R*o = 0.42%) and HET (*Ro* = 0.49%) at 41 and 39 Ma, respectively, and the
438 corresponding burial depths were 1250 and 1600 m, respectively. The kerogen of Es3
439 source rock is dominated by type II_1, and the required maturity for HGE becomes larger.
440 Therefore, only the lower source rock of the Es3 member generated and expelled
441 hydrocarbons at ~32 and ~24 Ma, respectively, and the corresponding burial depths
442 were 1980 and 2470 m, respectively. The Es1 source rock has not reached the HET (**Fig.**
443 **15a**).

444 The SS3 well had experienced continuous deep burial and reached a maximum
445 maturity of *R*o = 1.48%. The Es4 source rock is type II_2 kerogen, which reached the
446 HGT (*R*o = 0.62%) and HET (*R*o = 0.69%) at 40.2 and 39.5 Ma, respectively. The Es3
447 source rock is also type II_2, which reached the HGT and HET at 38.5 and 37.8 Ma,
448 respectively. Alternatively, the Es1 source rock is type I, which made the onsets of the
449 HGE of the Es1 source rock advance to 29 and 27.5 Ma (**Fig. 15b**).

450

451 **Fig. 15**. Simulated burial and thermal history of Shahejie Formation in the Liaohe
452 Western Depression. (a) Well Shu123. (b) Well SS3.

453 5.3. Reliability of *TOC* recovery of different kerogen types

454 **Fig. 16** illustrates the variations of the *TOC* recovery coefficient (*K*) obtained
455 using different methods with increasing maturity. As shown in **Fig. 16a**, K_1 is obtained
456 by the pyrolysis experiment, which represents the ratio of the TOC_o to the residual *TOC*
457 at each simulated temperature. When *R*o = 0.50%, the K_1 of types I, II_1, II_2, and III
458 source rocks starts to increase. Then, the increase of K_1 value becomes rapidly and then
459 gradually slows down with the increasing maturity. The maximum K_1 of types I, II_1, II_2,
460 and III source rocks can reach 3.05, 2.00, 1.50, and 1.25, respectively. In this study, K_2

461 is recovered using Eq. (10). The maximum K_2 of I, II_1, II_2, and III source rocks can
462 reach 2.92, 1.74, 1.29, and 1.05, respectively, which is comparable to the previous study
463 (Zhu et al., 2022; **Fig. 16b**). The T_R and f of organic matter are considered in the
464 recovery of TOC_o in this study, which makes the K value slightly smaller than that in
465 the pyrolysis experiment.
466
467 **Fig. 16**. Variation of *TOC* recovery coefficient K with the increasing maturity. (a) K_1
468 obtained by the hydrocarbon generation thermal simulation (according to Liaohe
469 Oilfield Company). (b) K_2 obtained by Eqs. (10) and (11).

470 5.4. Assessment of hydrocarbon resource potentials

471 The HGE capacities of Shahejie lacustrine source rocks are quantitatively
472 characterized. In combination with the effective thickness (H), *TOC*, and density of the
473 source rocks, the hydrocarbon generation intensity (I_g) and hydrocarbon expulsion
474 intensity (I_e) are calculated, as shown in **Fig. 17**. From the Es4 to the Es1 members, the
475 center of I_g and I_e gradually shifted from north to south. The I_g and I_e of the Es3 source
476 rock are very large because of the extensive effective thickness and high maturity and
477 can be greater than 5000×10^4 t/km^2 in the Qingshui sag. According to Eqs. (10)–(15),
478 the maximum hydrocarbon generation amount (Q_g) of Es1, Es3, and Es4 source rocks
479 can reach 149.35×10^8 t, 545.68×10^8 t, and 125.75×10^8 t, respectively. The
480 hydrocarbon expulsion amount (Q_e) of Es1, Es3, and Es4 source rocks can reach 40.05
481 $\times 10^8$ t, 418.35×10^8 t, and 29.86×10^8 t, respectively. The residual hydrocarbon amount
482 (Q_r) can reach 109.31×10^8 t, 127.33×10^8 t, and 95.89×10^8 t, respectively.
483 Under the control of buoyancy, the expelled hydrocarbons migrate to traps with
484 good physical properties to form conventional hydrocarbon resources (White, 1885) or
485 migrate to tight reservoirs to form tight hydrocarbon resources (Shanley et al., 2004;

Pang et al., 2021). Residual hydrocarbons remain in place to form shale oil/gas resources (Masters, 1979). In accordance with the Third Resource Evaluation of Liaohe Oilfield Company, the hydrocarbon accumulation coefficients of conventional/tight hydrocarbon resources and shale oil resources are chosen as 9.6% and 19.0%, respectively. The coefficients of mobility of conventional/tight hydrocarbon resources and shale oil resources are chosen as 30.3% and 28.6%, respectively (Jarvie, 2012). Additionally, 10%, 20%, and 40% of the recoverable coefficients represent the realistic, expected, and prospective resources, respectively.

As shown in **Fig. 18**, the realistic conventional/tight hydrocarbon resources in the Es3 member can reach 1.21×10^8 t, and the realistic shale oil resources can reach 0.69×10^8 t. The realistic conventional/tight hydrocarbon resources of Es1 and Es4 members are 0.12×10^8 t and 0.09×10^8 t, respectively, and the realistic resources of shale oil resources are 0.59×10^8 t and 0.52×10^8 t, respectively, thereby offering great unconventional shale oil and gas exploration prospects. It must be noted that the resource evaluation results are highly dependent on geological data. The accuracy of the resource evaluation results will improve with the improvement of basic geological data.

Fig. 17. HGE intensities of Shahejie lacustrine source rocks in the Liaohe Western Depression.

Fig. 18. Evaluation of different types and different levels of oil/gas resources. (a) Es1 member. (b) Es3 member. (c) Es4 member.

6. Conclusion

In this study, the data-driven HGE models of source rocks with different kerogen

types were established using abundant Rock-Eval/*TOC*/*R*o datasets. By integrating conventional geochemical analysis, numerical analysis, hydrocarbon generation kinetics, and basin modeling, the capacity and history of the HGE of source rocks with different kerogen types were revealed. The main conclusions of this study are as follows:

(1) From the perspective of Es4, Es3, to Es1 source rocks, the *TOC* contents gradually decrease, and the kerogen types are predominantly types I–II_1, II_1–II_2, and II–III, respectively. The Es3 source rock ranges from low mature to high mature. The Es4 and Es1 source rocks are low-mature to mature. The laminated texture was developed in Shahejie lacustrine source rocks.

(2) The hydrocarbon generation kinetics of Es4, Es3, and Es1 source rocks exhibit differences. The *E* of types I and II_1 kerogen is concentrated in 180~200 kcal/mol. The *E* of type II_2 kerogen is concentrated in 220~240 kcal/mol. While the *E* of type III kerogen has a wide range of 150~280 kcal/mol, indicating that its chemical structure is more complex than that of types I–II kerogen.

(3) The optimized HGE models of source rocks with different kerogen types are established. The GPI_o of types I, II_1, II_2, and III source rocks is 790, 510, 270, and 85 mg/g *TOC*, respectively. The HGTs of types I, II_1, II_2, and III source rocks are 0.42% *R*o, 0.50% *R*o, 0.62% *R*o, and 0.74% *R*o, respectively. The HETs of types I, II_1, II_2, and III source rocks are 0.49% *R*o, 0.56% *R*o, 0.69% *R*o, and 0.87% *R*o, respectively. As the maturity increases, the hydrocarbons are generated and expelled quickly from types I and II_1 source rocks, and the OM is completely transformed at 1.20% *R*o. The T_R, E_R, r_g, and r_e of types II_2 and III source rocks are slower than types I and II_1 source rocks. The maximum *TOC* recovery coefficient (*K*) for types I, II_1, II_2, and III kerogen obtained in this study can reach 2.92, 1.74, 1.29, and 1.05, respectively.

(4) Different types (conventional/tight/shale oil and gas) and levels

(realistic/expected/perspective resources) of hydrocarbon resources of the Es4, Es3, and Es1 members are evaluated. Considering the accumulation, mobility, and recoverability coefficients, the Es3 member has considerable realistic conventional and unconventional hydrocarbon resources. The Es4 and Es1 members have considerable realistic unconventional shale oil resources.

Acknowledgements

This research is supported by the Joint Fund of the National Natural Science Foundation of China (grant number U19B6003-02), the Cooperation Program of PetroChina Liaohe Oilfield Company (grant Number HX20180604), and the AAPG Foundation Grants-in-Aid Program (grant number 22269437). This study has benefited considerably from PetroChina Liaohe Oilfield Company for data support. We also thank the editor and the anonymous reviewers for their professional suggestions and comments.

References

Behar, F., Kressmann, S., Rudkiewicz, J.L., Vandenbroucke, M., Eckardt, C.B., Maxwell, J.R., Larter, S.R., Manning, D.A.C., 1992. Experimental simulation in a confined system and kinetic modelling of kerogen and oil cracking. Org. Geochem. 19 (1-3), 173-189. https://doi.org/10.1016/0146-6380(92)90035-V.

Bordenave, M.L., Espitalie, J., Leplat, J.L., Vandenbroucke, M., 1993. Screening techniques for source rock evaluation. In: Bordenave, M.L. (Ed.), Appl. Petrol. Geochem. 217-278.

Braun, R.L., Burnham, A.K., 1987. Analysis of chemical reaction kinetics using a distribution of activation energies and simpler models. Energy. Fuel, 1, 153–161.

https://doi.org/10.1021/ef00002a003.

Chen, J.Q., Pang, X.Q., Pang, H., Chen, Z.H., Jiang, C.Q., 2018. Hydrocarbon evaporative loss evaluation of lacustrine shale oil based on mass balance method: Permian Lucaogou Formation in Jimusaer Depression, Junggar Basin. Mar. Petrol. Geol. 91, 422-431. https://doi.org/10.1016/j.marpetgeo.2018.01.021.

Chen, J.P., Sun, Y.G., Zhong, N.N., Huang, Z.K., Deng, C.P., Xie, L.J., Han, H., 2014. Hydrocarbon generation and expulsion efficiency and model of lacustrine source rocks under geological conditions. J. Geol. 88 (11), 2005-2032 (in Chinese with English abstract). doi:10.19762/j.cnki.dizhixuebao.2014.11.001.

Chen, J.Q., Zhang, X,G., Chen, Z.H., Pang, X.Q., Yang, H.J., Zhao, Z.F., Pang, B., Ma, K.Y., 2021. Hydrocarbon expulsion evaluation based on pyrolysis Rock-Eval data: Implications for Ordovician carbonates exploration in the Tabei Uplift, Tarim. J. Petrol. Sci. Eng. 196, 107614. https://doi.org/10.1016/j.petrol.2020.107614.

Chen, Z.H., Jiang, C.Q., 2015. A data driven model for studying kerogen kinetics with unconventional shale application examples from Canadian sedimentary basins. Mar. Pet. Geol. 67, 795–803. https://doi.org/10.1016/j.marpetgeo.2015.07.004.

Chen, Z.H., Jiang, C.Q., 2016. A revised method for organic porosity estimation in shale reservoirs using Rock-Eval data: Example from Duvernay Formation in the Western Canada Sedimentary Basin. AAPG Bull. 100 (03), 405-422. https://doi.org/10.1306/08261514173.

Chen, Z.H., Liu, X.J., Osadetz, K.G., 2019. Petroleum generation kinetic models for

Late Ordovician kukersite Yeoman Formation source rocks, Williston Basin (southern Saskatchewan), Canada. Fuel. 241, 234-246. https://doi.org/10.1016/j.fuel.2018.11.154.

Chen, Z.H., Qiao, R.Z., Li, C.Y., Wang, D.Y., Gao, Y., 2022. Hydrocarbon generation potential and model of the deep lacustrine source rocks in the Dongying Depression, Bohai Bay Basin. Mar. Petrol. Geol. 140, 105656. https://doi.org/10.1016/j.marpetgeo.2022.105656.

Chen, Z.H., Wang, T.G., Liu, Q., Zhang, S.C., Zhang, L.Y., 2015. Quantitative evaluation of potential organic-matter porosity and hydrocarbon generation and expulsion from mudstone in continental lake basins: A case study of Dongying sag, eastern China. Mar. Petrol. Geol. 66, 906-924. https://doi.org/10.1016/j.marpetgeo.2015.07.027.

Espitalie, J., Marquis, F., Barsony, I., 1984. Geochemical logging. In: Voorhess, K.J. (Ed.), Analytical Pyrolysis. Butterworths, Boston, pp. 53–79. https://doi.org/10.1016/B978-0-408-01417-5.50013-5.

Guo, X.W., Liu, K.Y., He, S., Song, G.Q., Wang, Y.S., Hao, X.F., Wang, B.J., 2012. Petroleum generation and charge history of the northern Dongying Depression, Bohai Bay Basin, China: Insight from integrated fluid inclusion analysis and basin modelling. Mar Petrol Geol 32, 21-35. https://doi.org/10.1016/j.marpetgeo.2011.12.007.

Guo, Y.C., Pang, X.Q., Dong, Y.X., Jiang, Z.X., Chen, D.X., Jiang, F.J., 2013. Hydrocarbon generation and migration in the Nanpu Sag, Bohai Bay Basin, eastern China: Insight from basin and petroleum system modeling. J Asian Earth

603 Sci 77, 140-150. https://doi.org/10.1016/j.jseaes.2013.08.033.

604 He, W.T., Sun, Y.H., Shan, X.L., 2021. Organic matter evolution in pyrolysis
605 experiments of oil shale under high pressure: Guidance for in situ conversion of
606 oil shale in the Songliao Basin. J. Anal. Appl. Pyrol. 155, 105091.
607 https://doi.org/10.1016/j.jaap.2021.105091.

608 Hu, T., Pang, X.Q., Jiang, F.J., Wang, Q.F., Liu, X.H., Wang, Z., Jiang, S., Wu, G.Y., Li,
609 C.J., Xu, T.W., Li, M.W., Yu, J.W., Zhang, C.X., 2021. Movable oil content
610 evaluation of lacustrine organic-rich shales: Methods and a novel quantitative
611 evaluation model. Earth-Sci. Rev. 214, 103545.
612 https://doi.org/10.1016/j.earscirev.2021.103545.

613 Hu, T., Pang, X.Q., Jiang, F.J., Zhang, C.X., Wu, G.Y., Hu, M.L., Jiang, L., Wang, Q.F.,
614 Xu, T.W., Hu, Y., Jiang, S., Wang, W.Y., Li, M.W., 2022a. Dynamic continuous
615 hydrocarbon accumulation (DCHA): Existing theories and a new unified
616 accumulation model. Earth-Sci. Rev. 232, 104109.
617 https://doi.org/10.1016/j.earscirev.2022.104109.

618 Hu, T., Wu, G.Y., Xu, Z., Pang, X.Q., Liu, Y., Yu, S., 2022b. Potential resources of
619 conventional, tight, and shale oil and gas from Paleogene Wenchang Formation
620 source rocks in the Huizhou Depression. Adv. Geo-Energy Res. 6, 402-414.
621 https://doi.org/10.46690/ager.2022.05.05.

622 Huang, D.F., Li, J.C., Zhang, D.J., 1984. Evolution and Hydrocarbon Generation
623 Mechanism of Continental Organic Matter. Beijing: Petroleum Industry Press (in
624 Chinese with English abstract).

625 Hui, S.S., Pang, X.Q., Liu, G.D., Zhou, X.L., Hu, T., Mei, S.X., 2022. Characteristics
626 of hydrocarbon source rocks and fine correlation of oil sources in Shahejie
627 Formation of Liaohe Western Depression. Geoscience 1-28 (in Chinese with
628 English abstract). doi:10.3799/dqkx.2022.090.
629 Hui, S.S., Pang, X.Q., Pang, H., Li, C.R., Zhou, X.L., Hu, T., Shi, K.Y., Li, M., Mei,
630 S.X., Yuan, W., Cheng, J.P., 2023. A Data-Driven Approach to the Unified
631 Evaluation of Conventional and Unconventional Hydrocarbon Resources:
632 Application to Low-Mature to Mature Source Rocks in the Liaohe Western
633 Depression. Minerals, 13, 390. https://doi.org/10.3390/min13030390.
634 Jarvie, D. M., 2012. Shale resource systems for oil/gas: part 2-shale-oil resource
635 systems. In: Breyer, J.A. (Ed.), Shale Reservoirs-Giant Resources for the 21st
636 Century: AAPG Mem, 97, p. 89-119. doi:10.1306/13321447M973489.
637 Jarvie, D.M., Hill, R.J., Ruble, T.E., Pollastro, R.M., 2007. Unconventional shale-gas
638 systems: The Mississippian Barnett Shale of north-central Texas as one model for
639 thermogenic shale-gas assessment. AAPG Bull. 91 (4), 475-499.
640 https://doi.org/10.1306/12190606068.
641 Justwan, H., Dahl, B., 2005. Quantitative hydrocarbon potential mapping and
642 organofacies study in the Greater Balder Area, Norwegian North Sea. In: Dore, A.
643 G. & Vining, B. A. (eds) Petroleum Geology: North-West Europe and Global
644 Perspectives—Proceedings of the 6th Petroleum Geology Conference, 1317–1329.
645 https://doi.org/10.1144/0061317.

646 Katz, B.J., Lin, F., 2014. Lacustrine basin unconventional resource plays: Key
647 differences. Mar. Pet. Geol. 56, 255–265.
648 https://doi.org/10.1016/j.marpetgeo.2014.02.013.
649 Li, C.R., Pang, X.Q., Huo, Z.P., Wang, E.Z., Xue, N., 2020. A revised method for
650 reconstructing the hydrocarbon generation and expulsion history and evaluating
651 the hydrocarbon resource potential: Example from the first member of the
652 Qingshankou Formation in the Northern Songliao Basin, Northeast China. Mar.
653 Petrol. Geol. 121, 104577. https://doi.org/10.1016/j.marpetgeo.2020.104577.
654 Li, Y.J., Song, L.H., Tang, Y.J., Zuo, J.P., Xue, D.J., 2022. Evaluating the mechanical
655 properties of anisotropic shale containing bedding and natural fractures with
656 discrete element modeling. Int. J. Coal Sci. Technol. 9, 18.
657 https://doi.org/10.1007/s40789-022-00473-5.
658 Ma, Z.L., Zheng, L.J., Xu, X.H., Bao, F., Yu, X.L., 2017. Thermal simulation
659 experiment of organic matter-rich shale and implication for organic pore formation
660 and evolution. Petrol. Res. 2 (4), 347-354.
661 https://doi.org/10.1016/j.ptlrs.2017.04.005.
662 Masters, J.A., 1979. Deep basin gas trap, Western Canada. AAPG Bull. 63, 152-181.
663 https://doi.org/10.1306/C1EA55CB-16C9-11D7-8645000102C1865D.
664 Modica, C.J., Lapierre, S.G., 2012. Estimation of kerogen porosity in source rocks as a
665 function of thermal transformation: example from the Mowry Shale in the Powder
666 River Basin of Wyoming. AAPG Bull. 96 (1), 87–108.

https://doi.org/10.1306/04111110201.

Pang, X.Q., Hu, T., Larter, S., Jiang, Z.X., Li, M.W., Wu, L.Y., Liu, K.Y., Jiang, S., Wang, W.Y., Hu, Q.H., Zhang, K., Li, Z., Bai, H., 2022. Hydrocarbon accumulation depth limit and implications for potential resources prediction. Gondwana Res. (103), 389-400. https://doi.org/10.1016/j.gr.2021.10.018.

Pang, X.Q., Jia, C.Z., Wang, W.Y., Chen, Z.X., Li, M.W., Jiang, F.J., Hu, T., Wang, K., Wang, Y.X., 2021. Buoyance-driven hydrocarbon accumulation depth and its implication for unconventional resource prediction. Geosci. Front. 12 (4), 101133. https://doi.org/10.1016/j.gsf.2020.11.019.

Pang, X.Q., Jia, C.Z., Zhang, K., Li, M.W., Wang, Y.W., Peng, J.W., Li, B.Y., Chen, J.Q., 2020. The dead line for oil and gas and implication for fossil resource prediction. Earth Syst. Sci. Data 12 (1), 577-590. https://doi.org/10.5194/essd-12-577-2020.

Pang, X.Q., Li, M.W., Li, S.M., Jin, Z.J., 2005. Geochemistry of petroleum systems in the Niuzhuang South Slope of Bohai Bay Basin: Part 3. Estimating hydrocarbon expulsion from the Shahejie formation. Org. Geochem. 36, 497–510. https://doi.org/10.1016/j.orggeochem.2004.12.001.

Peng, J.W., Pang, X.Q., Shi, H.S., Peng, H.J., Xiao, S., Yu, Q.H., Wu, L.Y., 2016. Hydrocarbon generation and expulsion characteristics of Eocene source rocks in the Huilu area, northern Pearl River Mouth basin, South China Sea: Implications for tight oil potential. Mar. Petrol. Geol. 72, 463-487.

https://doi.org/10.1016/j.marpetgeo.2016.02.006.

Peters, K., Burnham, A.K., Walters, C.C., 2015. Petroleum generation kinetics: single versus multiple heating-ramp open-system pyrolysis. AAPG Bull. 99 (4), 591–616. https://doi.org/10.1306/11141414080.

Peters, K.E., 1986. Guidelines for evaluating petroleum source rock using programmed pyrolysis. AAPG Bull. 70, 318–329. https://doi.org/10.1306/94885688-1704-11D7-8645000102C1865D.

Petersen, H.I., Bojesen-Koefoed, J.A., Mathiesen, A., 2010. Variations in composition, petroleum potential and kinetics of Ordovician-Miocene type I and type I-II source rocks (oil shales): implications for hydrocarbon generation characteristics. J. Pet. Geo. 33, 19-42. https://doi.org/10.1111/j.1747-5457.2010.00462.x.

Riediger, C., Carrelliand, G.G., Zonneveld, J.P., 2004. Hydrocarbon source rock characterization and thermal maturity of the Upper Triassic Baldonnel and Pardonet formations, northeastern British Columbia, Canada. B. Can. Petrol. Geol. 52, 277-301. https://doi.org/10.2113/52.4.277.

Shanley, K.W., Cluff, R.M., Robinson, J.W., 2004. Factors controlling prolific gas production from low-permeability sandstone reservoirs: Implications for resource assessment, prospect development, and risk analysis. AAPG Bull. 88, 1083-1121. https://doi.org/10.1306/03250403051.

Snowdon, L.R., 1991. Oil from Type III organic matter: resinite revisited. Org. Geochem. 17, 743-747. https://doi.org/10.1016/0146-6380(91)90018-F.

709 Shi, K.Y., Chen, J.Q., Pang, X.Q., Jiang, F.J., Hui, S.S., Pang, H., Ma, K.Y., Cong, Q.,
710 2022. Effect of wettability of shale on CO2 sequestration with enhanced gas
711 recovery in shale reservoir: Implications from molecular dynamics simulation. J.
712 Nat. Gas. Sci. Eng. 107, 104798. https://doi.org/10.1016/j.jngse.2022.104798.
713 Tegelaar, E.W., Noble, R.A., 1994. Kinetics of hydrocarbon generation as a function of
714 the molecular structure of kerogen as revealed by pyrolysis-gas chromatography.
715 Org. Geochem. 22, 543–574. https://doi.org/10.1016/0146-6380(94)90125-2.
716 Tissot, B.P., Welte, D.H., 1984. Petroleum Formation and Occurrence. Springer-Verlag.
717 Tong, H.M., Yu, F.S., Geng, C.B., 2008. Characteristics and evolution of strike-slip
718 tectonics of the Liaohe Western Sag, Bohai Bay Basin. Petrol. Sci. 5 (3), 223-229.
719 https://doi.org/10.1007/s12182-008-0034-0.
720 Ungerer, P., 1990. State of the art of research in kinetic model of oil formation and
721 expulsion.Org. Geochem. 16, 1–25. https://doi.org/10.1016/0146-6380(90)90022-
722 R.
723 Wang, E.Z., Feng, Y., Guo, T.L., Li, M.W., 2022. Oil content and resource quality
724 evaluation methods for lacustrine shale: A review and a novel three-dimensional
725 quality evaluation model. Earth-Sci. Rev. 232, 104134.
726 https://doi.org/10.1016/j.earscirev.2022.104134.
727 Wang, E.Z., Liu, G.Y., Pang, X.Q., Li, C.R., Zhao, Z.F., Feng, Y., Wu, Z.Y., 2020. An
728 improved hydrocarbon generation potential method for quantifying hydrocarbon
729 generation and expulsion characteristics with application example of Paleogene

730 Shahejie Formation, Nanpu Sag, Bohai Bay Basin. Mar. Petrol. Geol. 112, 104106.
731 https://doi.org/10.1016/j.marpetgeo.2019.104106.
732 Wang, M., Lu, S.F., Xue, H.T., 2011. Kinetic simulation of hydrocarbon generation
733 from lacustrine type I kerogen from the Songliao Basin: Model comparison and
734 geological application. Mar. Petrol. Geol. 28 (9), 1714-1726.
735 https://doi.org/10.1016/j.marpetgeo.2011.07.004.
736 Wei, Z.F., Zou, Y.R., Cai, Y.L., Wang, L., Luo, X.R., Peng, P.A., 2012. Kinetics of oil
737 group-type generation and expulsion: An integrated application to Dongying
738 Depression, Bohai Bay Basin, China. Org. Geochem. 52, 1-12.
739 https://doi.org/10.1016/j.orggeochem.2012.08.006.
740 White, I.C., 1885. The geology of natural gas. Science 6 (128), 42–44.
741 https://doi.org/10.1126/science.ns-5.125.521.
742 Yang, M.H., Zuo, Y.H., Yan, K.N., Zhou, Y.S., Zhang, Y.X., Zhang, C.F., 2022.
743 Hydrocarbon generation history constrained by thermal history and hydrocarbon
744 generation kinetics: A case study of the Dongpu Depression, Bohai Bay Basin,
745 China. Petrol. Sci. 19, 472-485. https://doi.org/10.1016/j.petsci.2021.10.009.
746 Yang, Z., Zou, C.N., Gu, Z.D., Yang, F., Li, J.R., Wang, X.N., 2022. Geological
747 characteristics and main challenges of onshore deep oil and gas development in
748 China. Adv. Geo-Energy Res. 6(3): 264–266.
749 https://doi.org/10.46690/ager.2022.03.09.
750 Zhang, Y.P., Li, Y.H., Guo, W., Li, Y.H., Dang, H.L., 2020. Differential evolution and
751 the influencing factors of low-maturity terrestrial shale with different types of

752 kerogen: A case study of a Jurassic shale from the northern margin of Qaidam
753 Basin, China. Int. J. Coal Geol. 230, 103591.
754 https://doi.org/10.1016/j.coal.2020.103591.
755 Zhang, Z., Bao, Z.D., Tong, H.M., Wang, Y., Li, H.W., 2013. Tectonic evolution and its
756 control over deposition in fault basins: A case study of the Western Sag of the
757 Cenozoic Liaohe Depression, eastern China. Petrol. Sci. 10 (3), 269-281.
758 https://doi.org/10.1007/s12182-013-0276-3.
759 Zhao, X.Z., Zhou, L.H., Pu, X.G., Jin, F.M., Shi, Z.N., Han, W.Z., Jiang, W.Y., Han,
760 G.M., Zhang, W., Wang, H., Ma, J.Y., 2020. Formation conditions and enrichment
761 model of retained petroleum in lacustrine shale: A case study of the Paleogene in
762 Huanghua depression, Bohai Bay Basin, China. Petrol. Explor. Dev. 47, 916-930.
763 https://doi.org/10.1016/S1876-3804(20)60106-9.
764 Zheng, D.Y., Pang, X.Q., Ma, X.H., Li, C.R., Zheng, T.Y., Zhou, L.M., 2019.
765 Hydrocarbon generation and expulsion characteristics of the source rocks in the
766 third member of the Upper Triassic Xujiahe Formation and its effect on
767 conventional and unconventional hydrocarbon resource potential in the Sichuan
768 Basin. Mar. Petrol. Geol. 109, 175-192.
769 https://doi.org/10.1016/j.marpetgeo.2019.06.014.
770 Zhu, C.Z., Gang, W.Z., Li, X.F., Wang, N., Guo, Y., Zhao, X.Z., Wang, Y.F., Pu, X.G.,
771 2022. The sorting effect of hydrodynamics on the geochemical compositions of
772 sedimentary organic matter in a lacustrine rift basin: Significance for hydrocarbon

773 exploration on the Qibei slope, Bohai Bay Basin, China. Mar. Petrol. Geol. 141,
774 105705. https://doi.org/10.1016/j.marpetgeo.2022.105705.
775 Zou, C.N., Yang, Z., He, D.B., Wei, Y.S., Li, J., Jia, A.L., Chen, J.J., Zhao, Q., Li, Y.L.,
776 Li, J., Yang, S., 2018. Theory, technology and prospects of conventional and
777 unconventional natural gas. Pet. Explor. Dev. 45 (4), 575–587.
778 https://doi.org/10.1016/S1876-3804(18)30066-1.
779 Zou, C.N., Zhu, R.K., Chen, Z.Q., Ogg, J.G., Wu, S.T., Dong, D.Z., Qiu, Z., Wang,
780 Y.M., Wang, L., Lin, S.H., Cui, J.W., Su, L., Yang, Z., 2019. Organic-matter-rich
781 shales of China. Earth-Sci. Rev. 189, 51-78.
782 https://doi.org/10.1016/j.earscirev.2018.12.002.
783

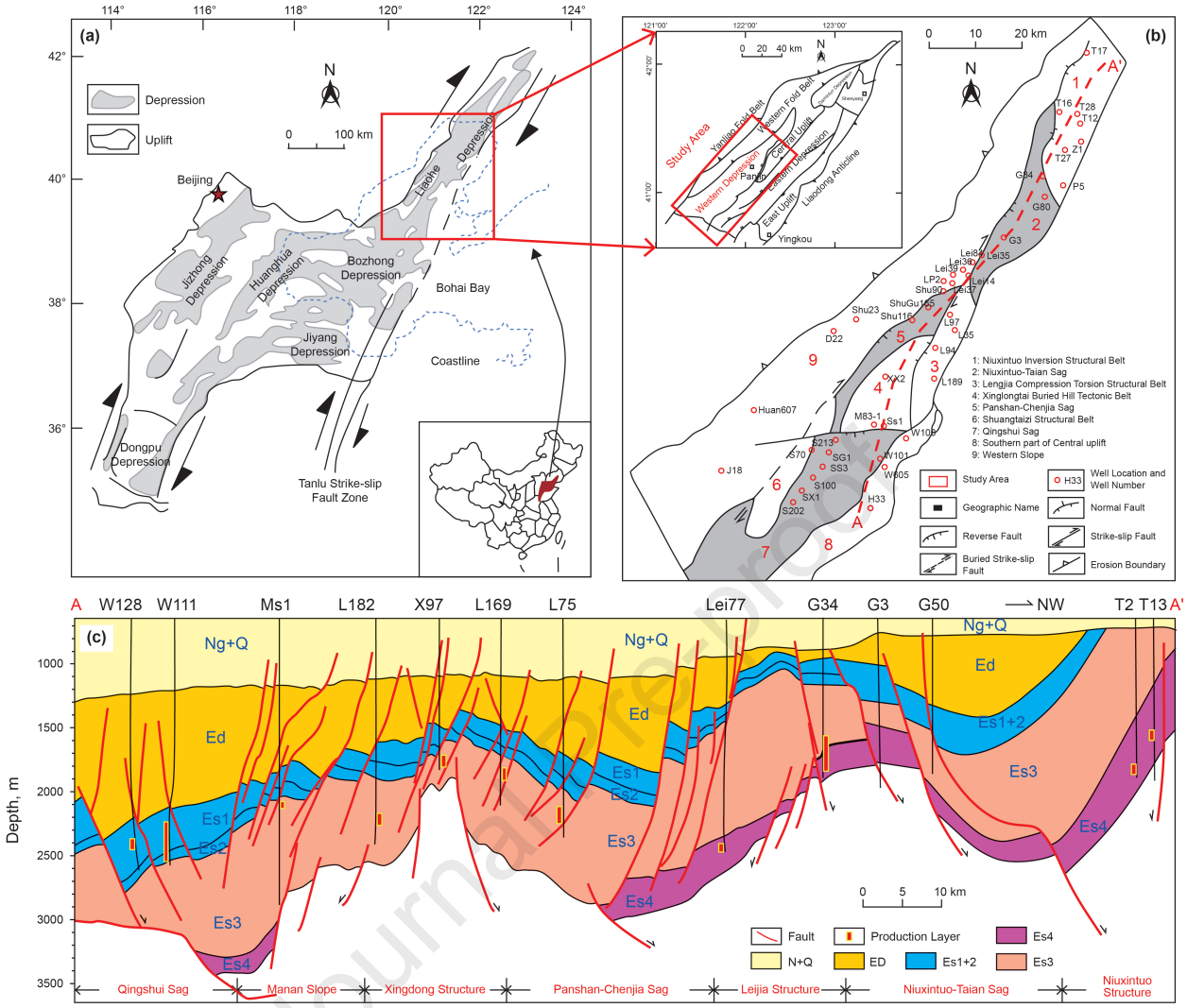

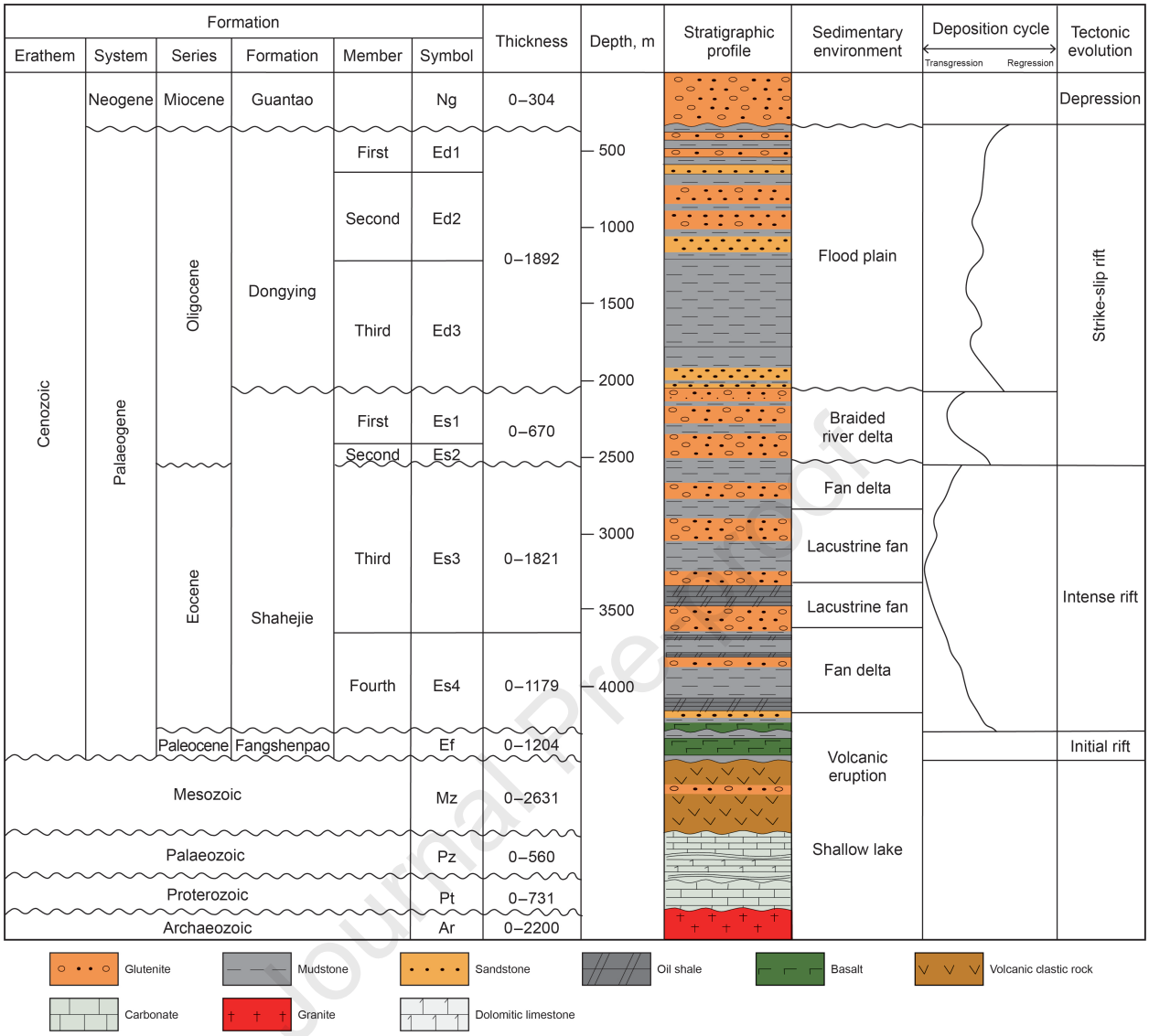

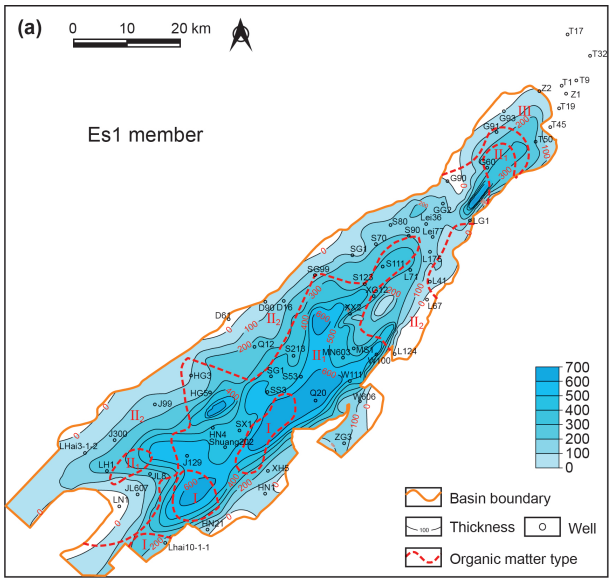

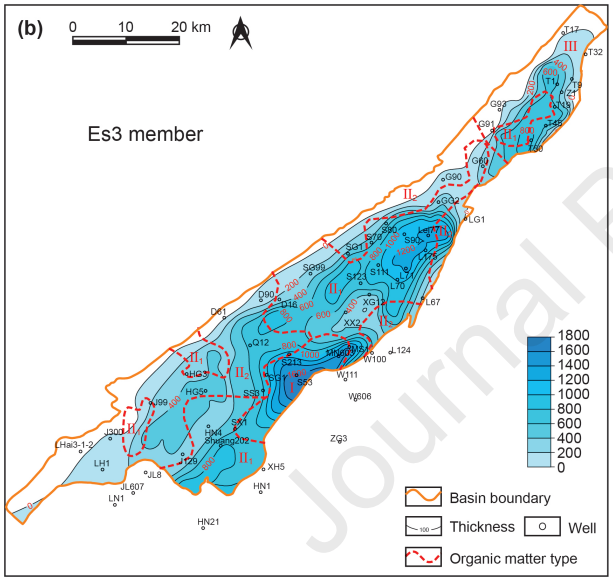

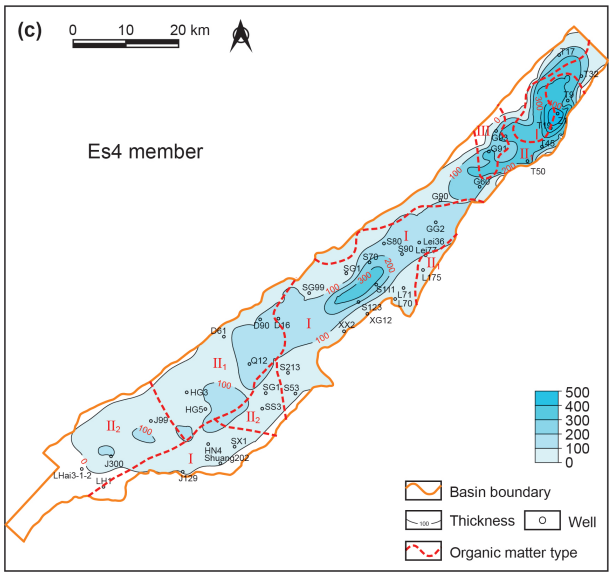

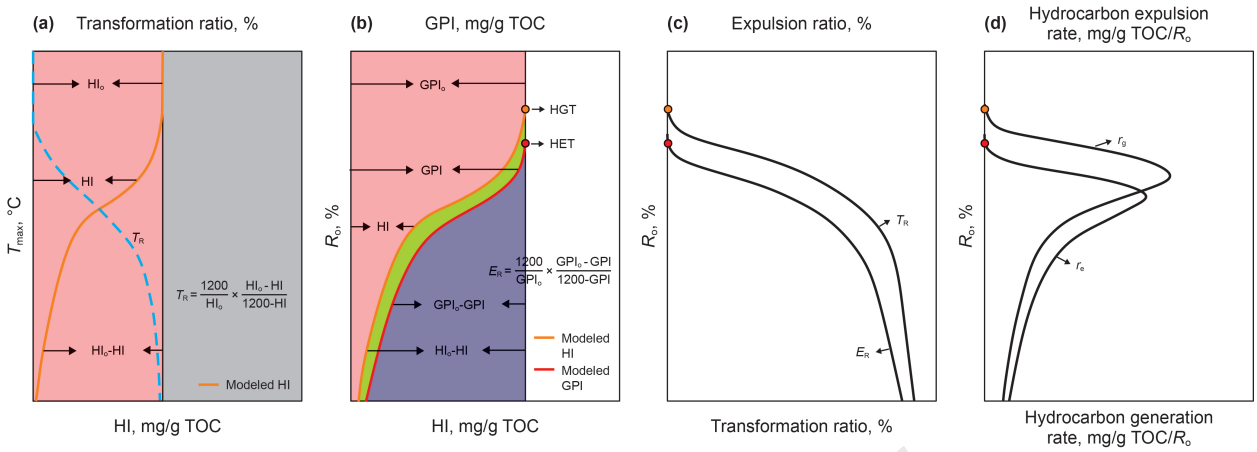

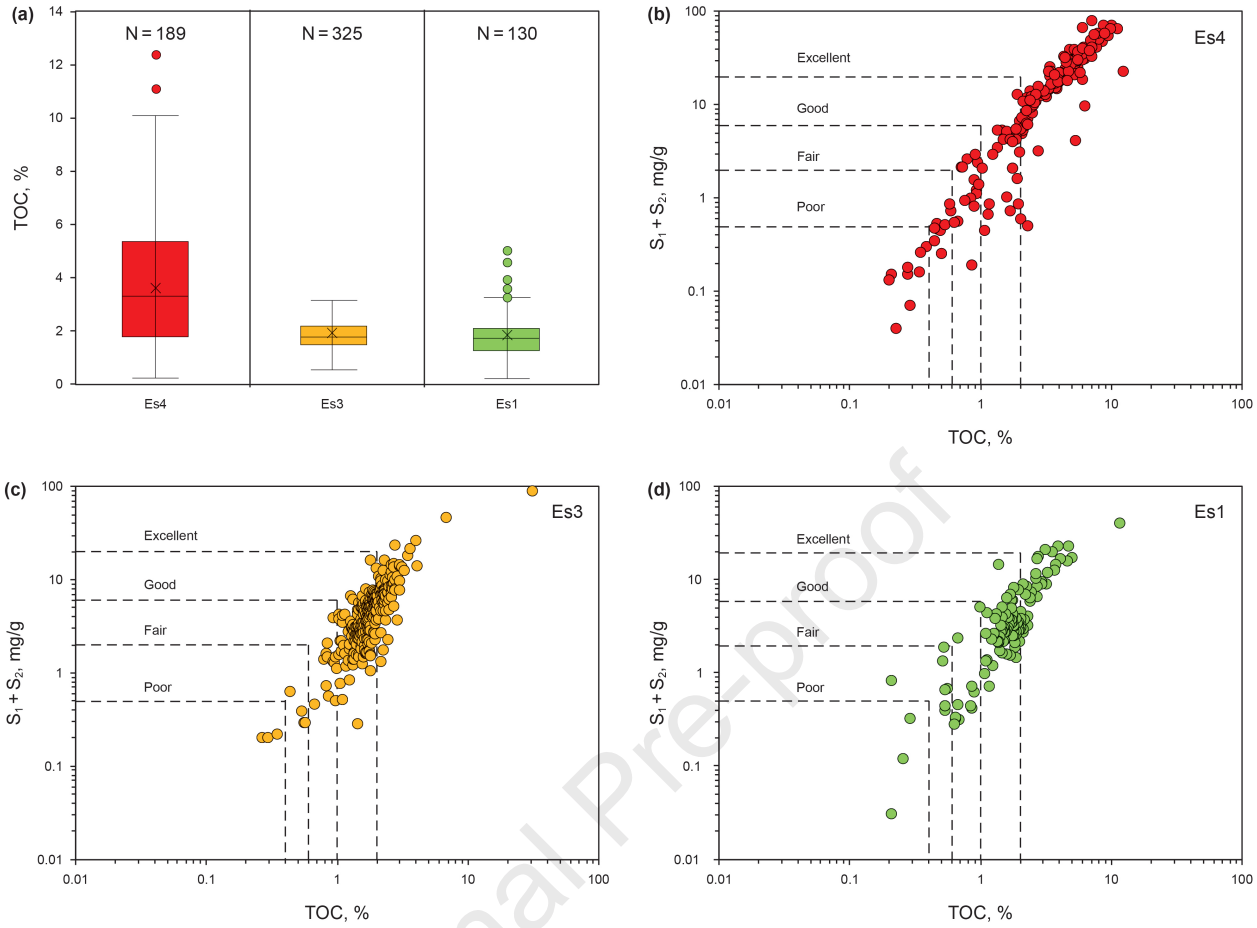

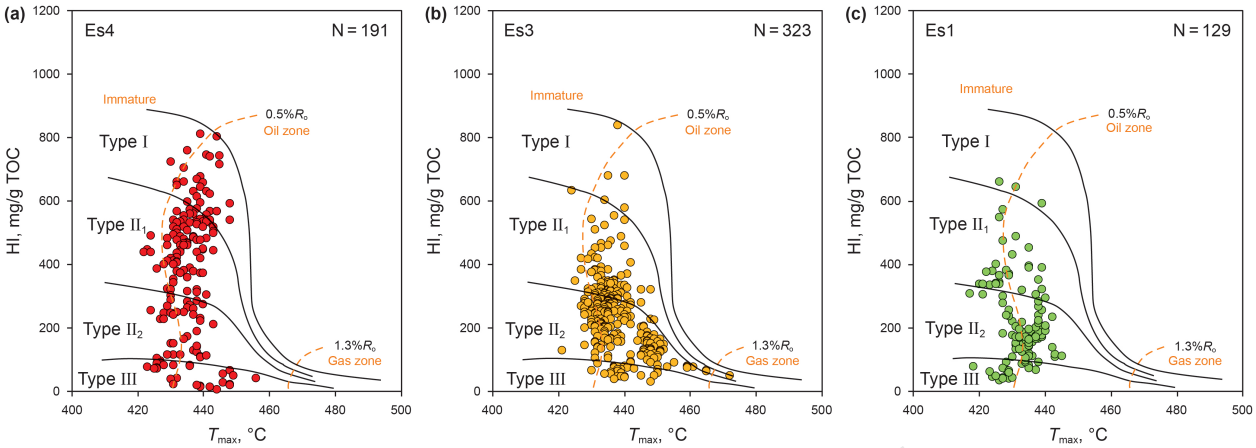

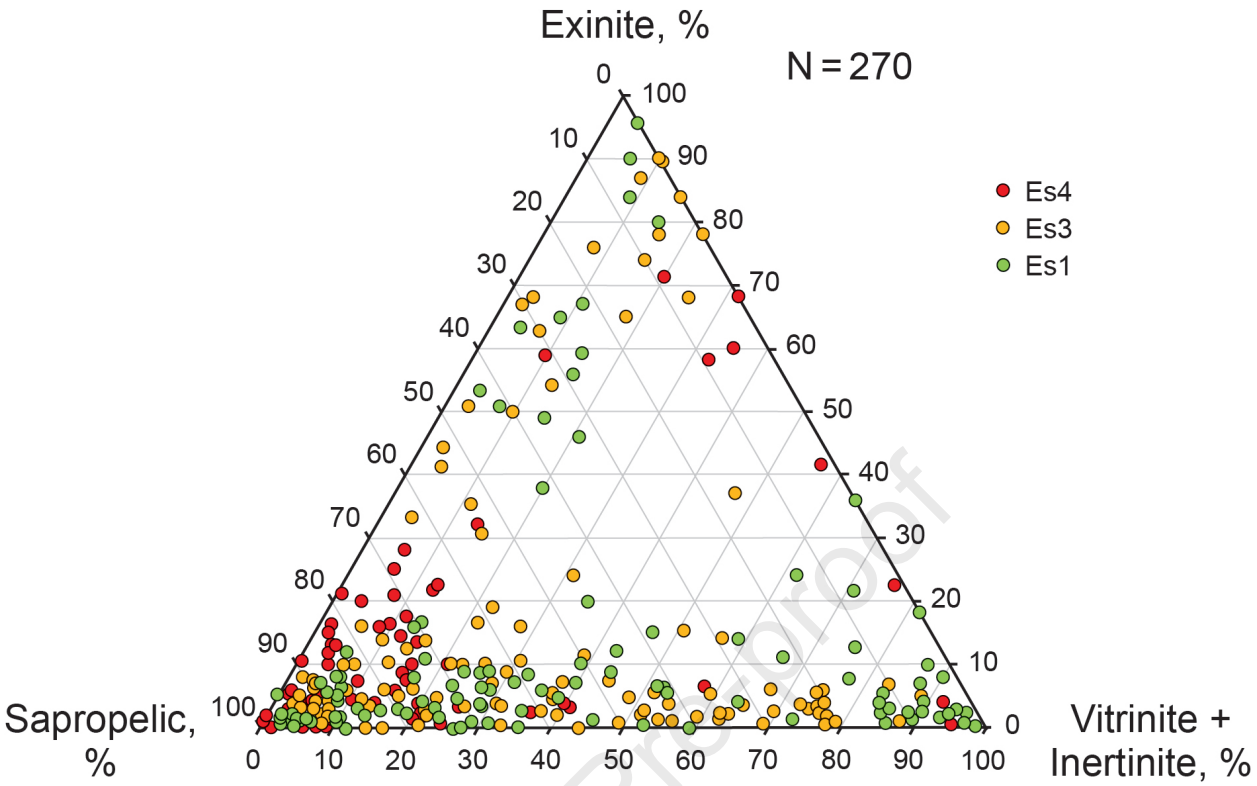

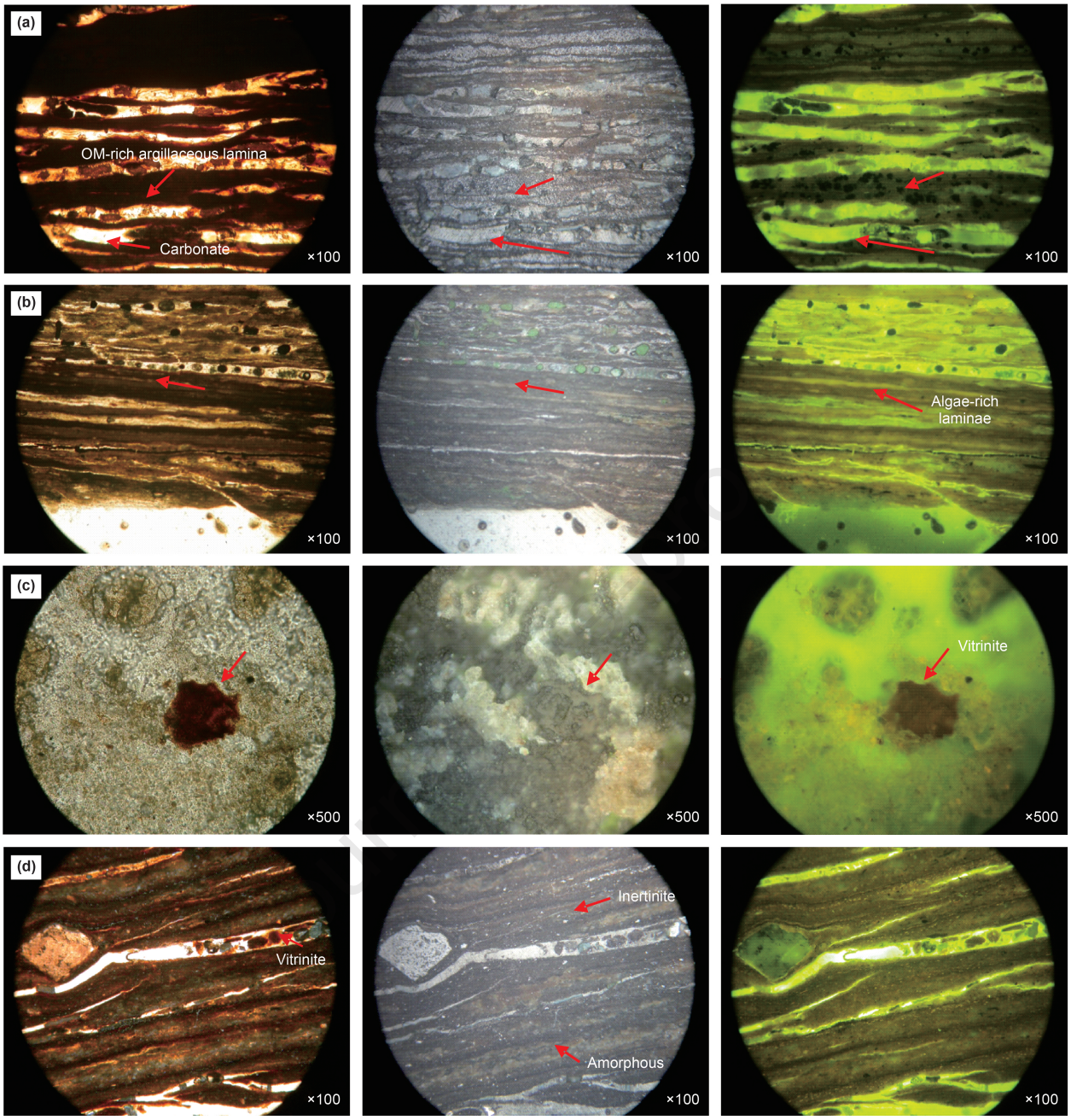
(a)
OM-rich argillaceous lamina
Carbonate
×100
×100
×100
(b)
×100
×100
Algae-rich laminae
×100
(c)
×500
×500
Vitrinite
×500
(d)
Vitrinite
×100
Inertinite
Amorphous
×100
×100

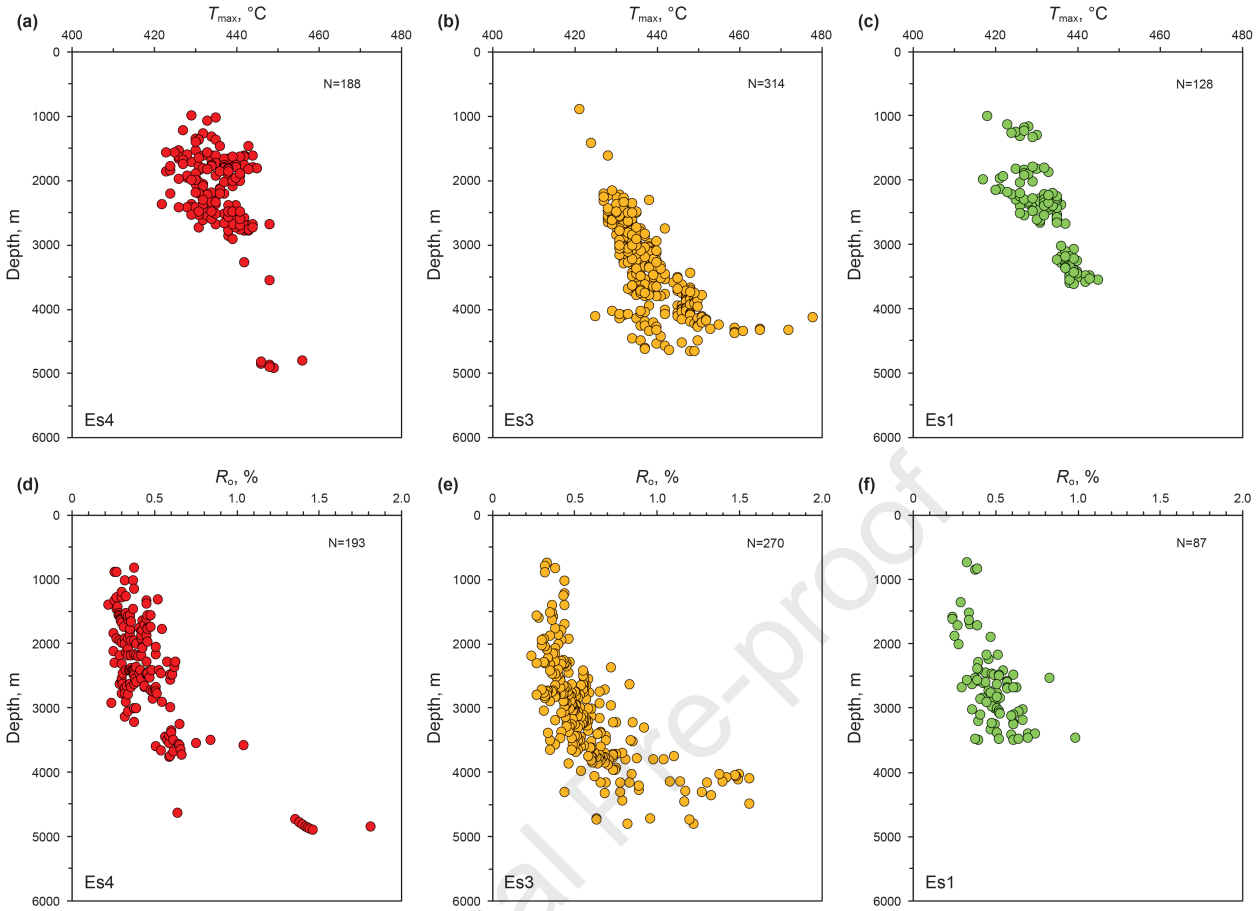

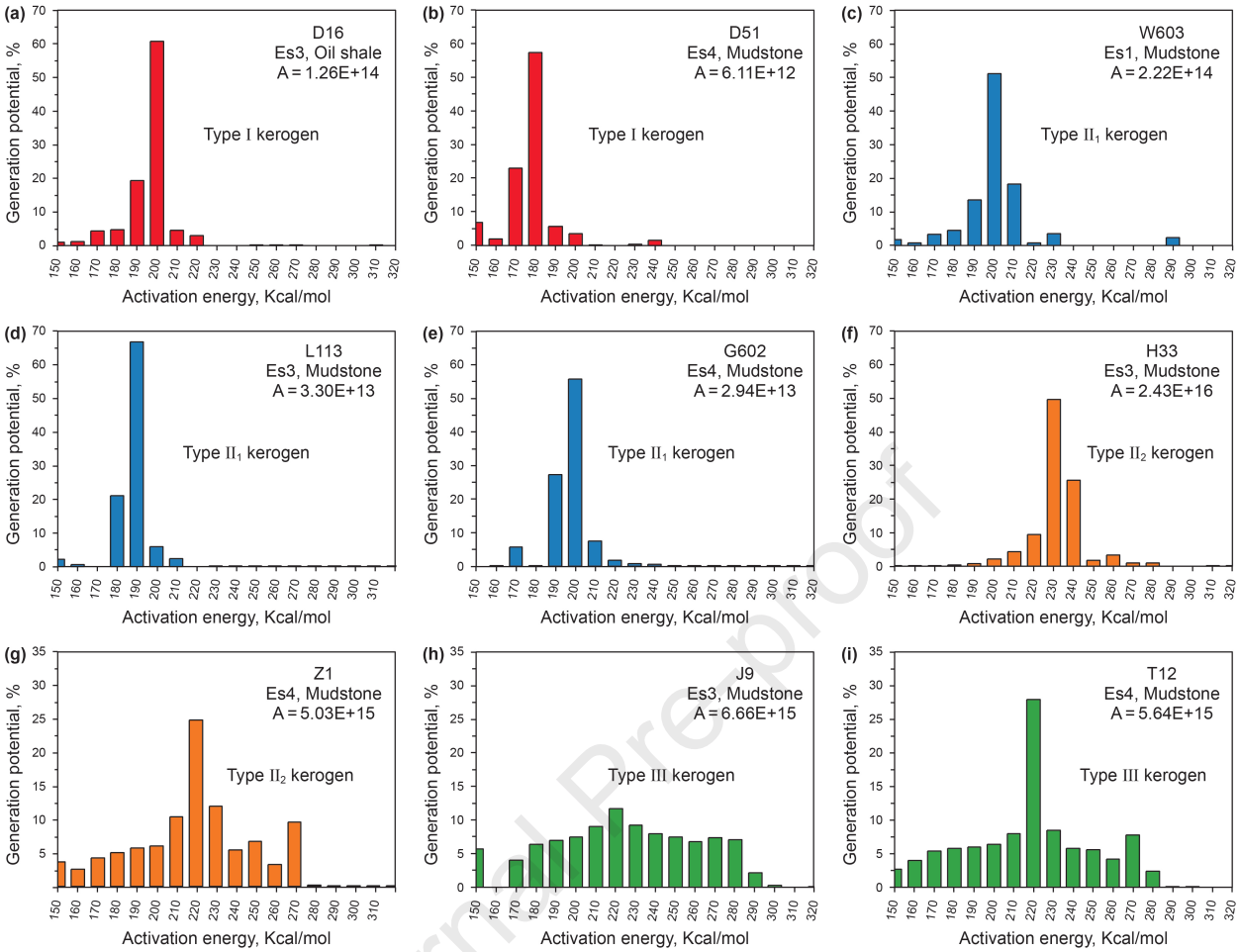

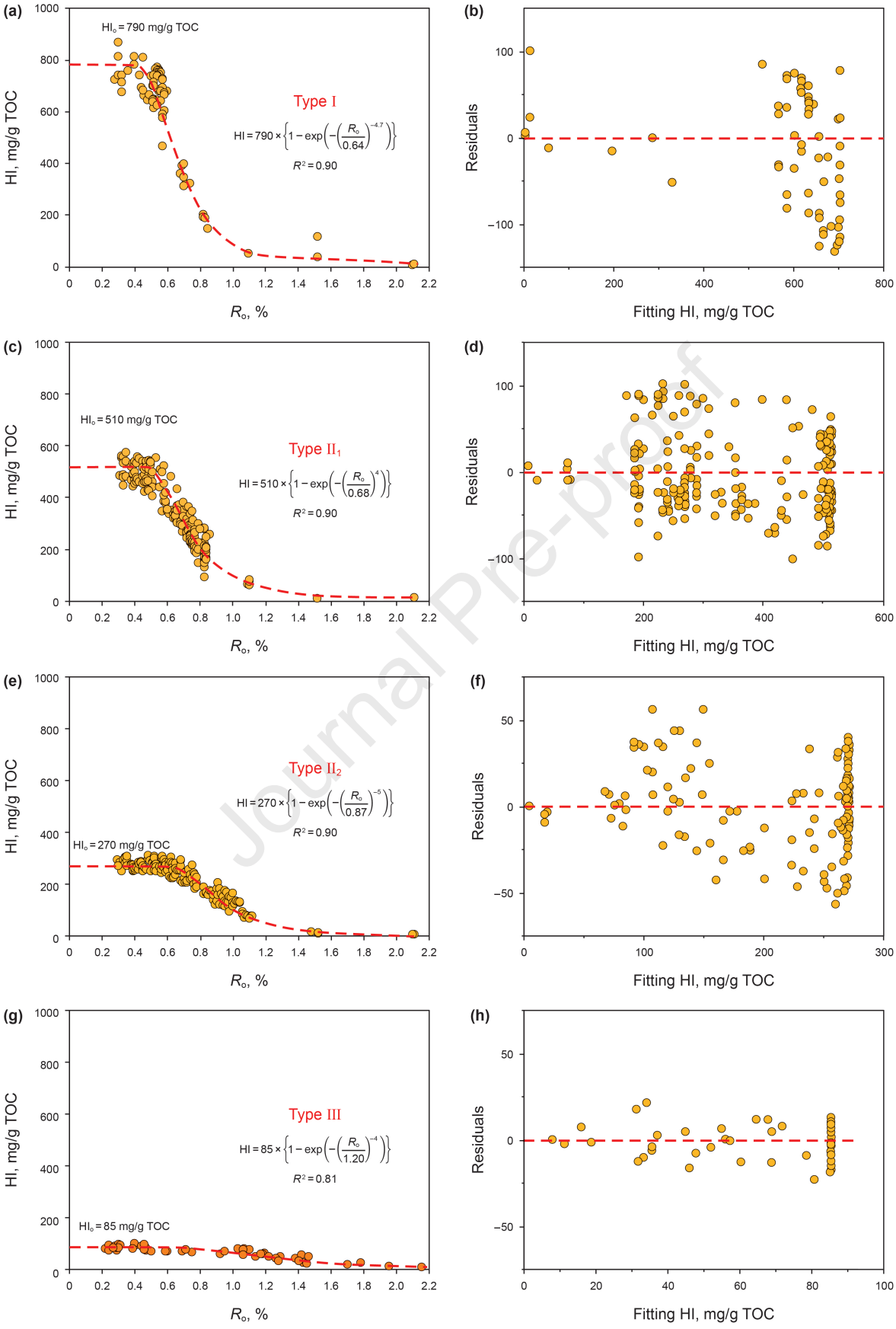

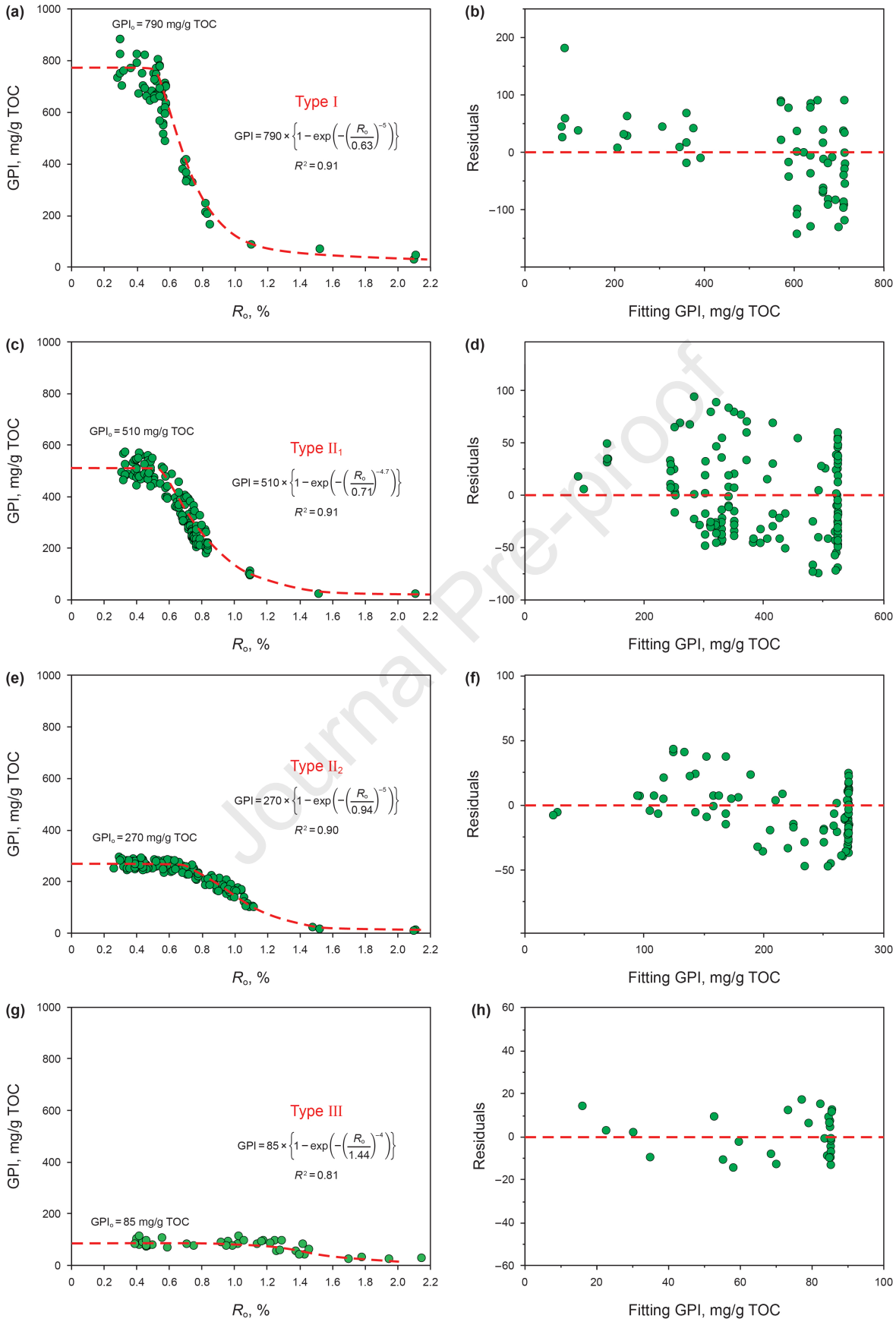

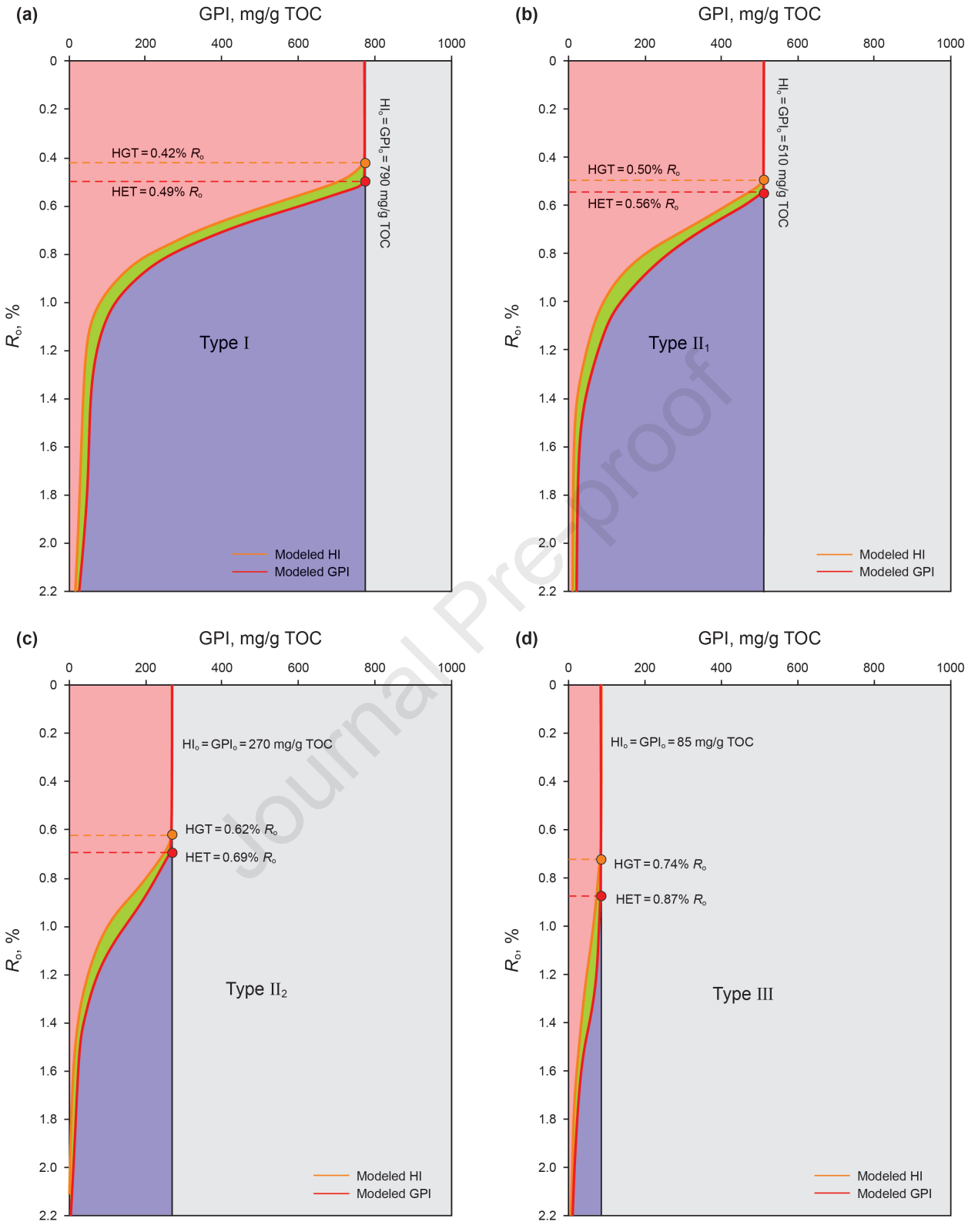

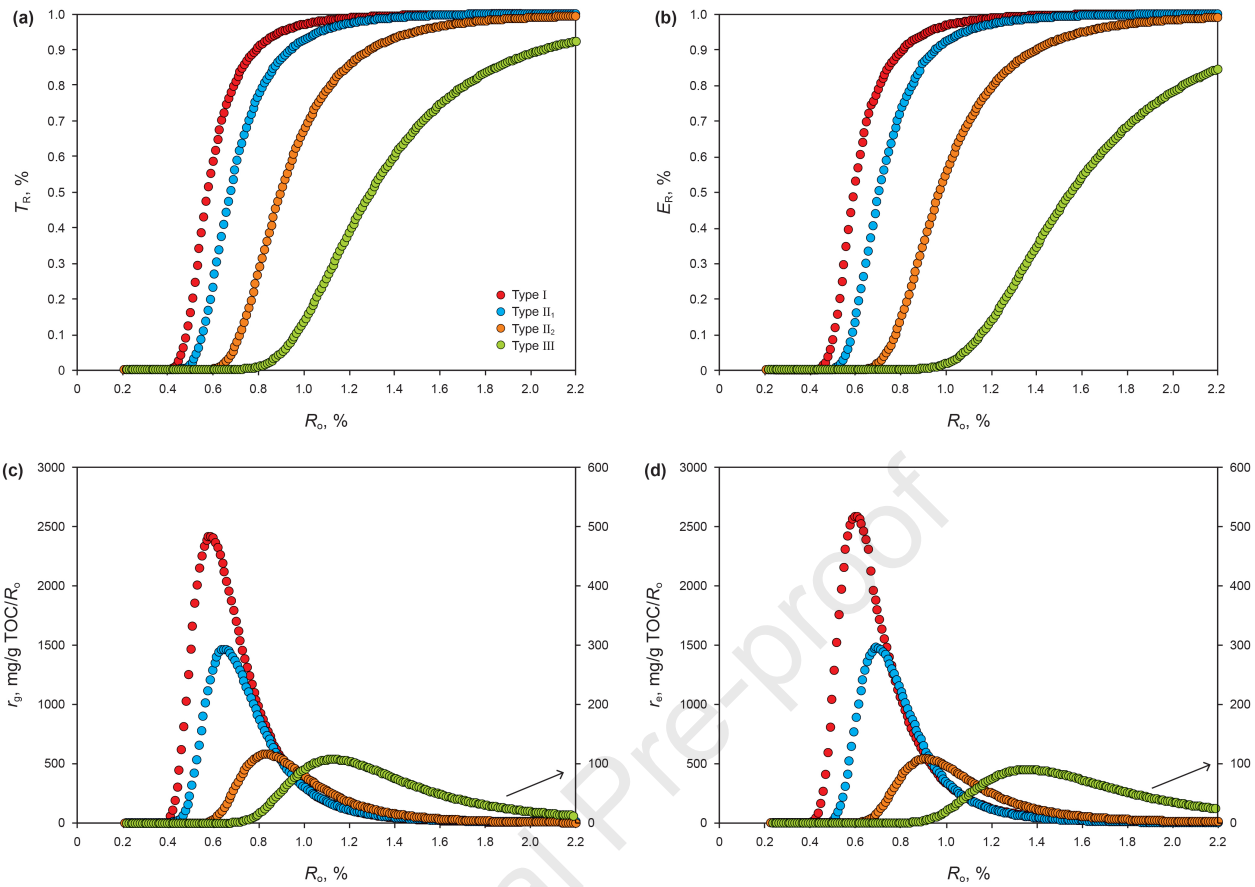

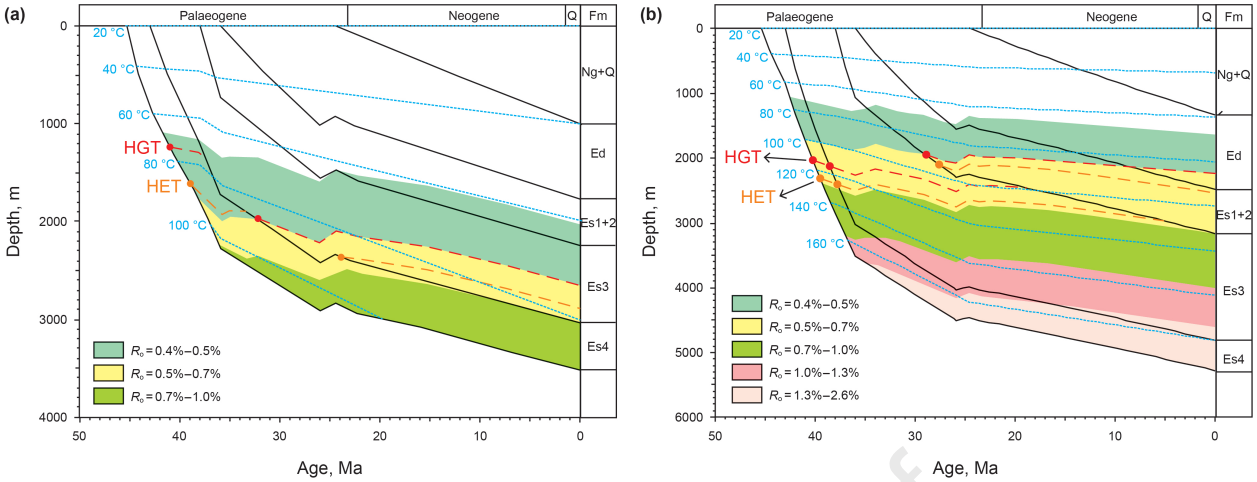

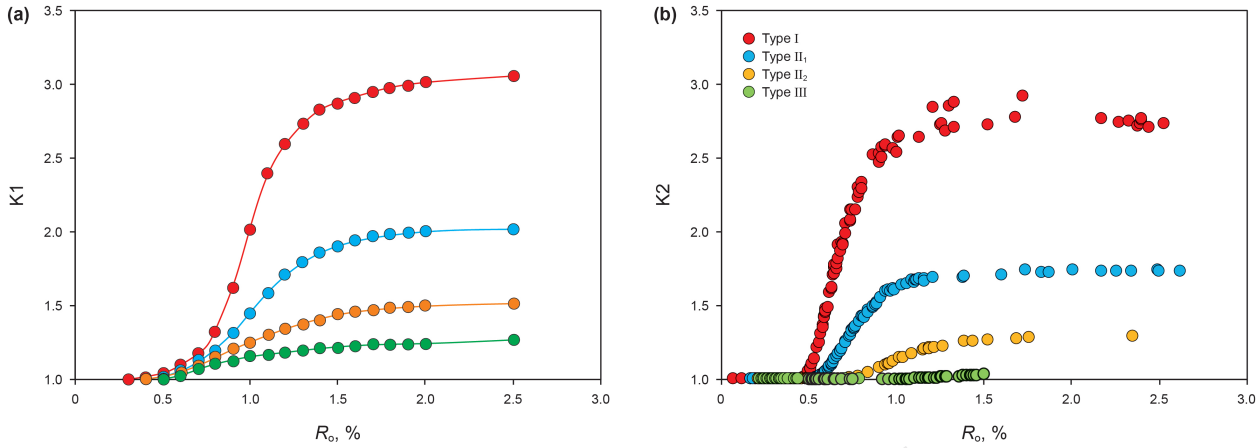

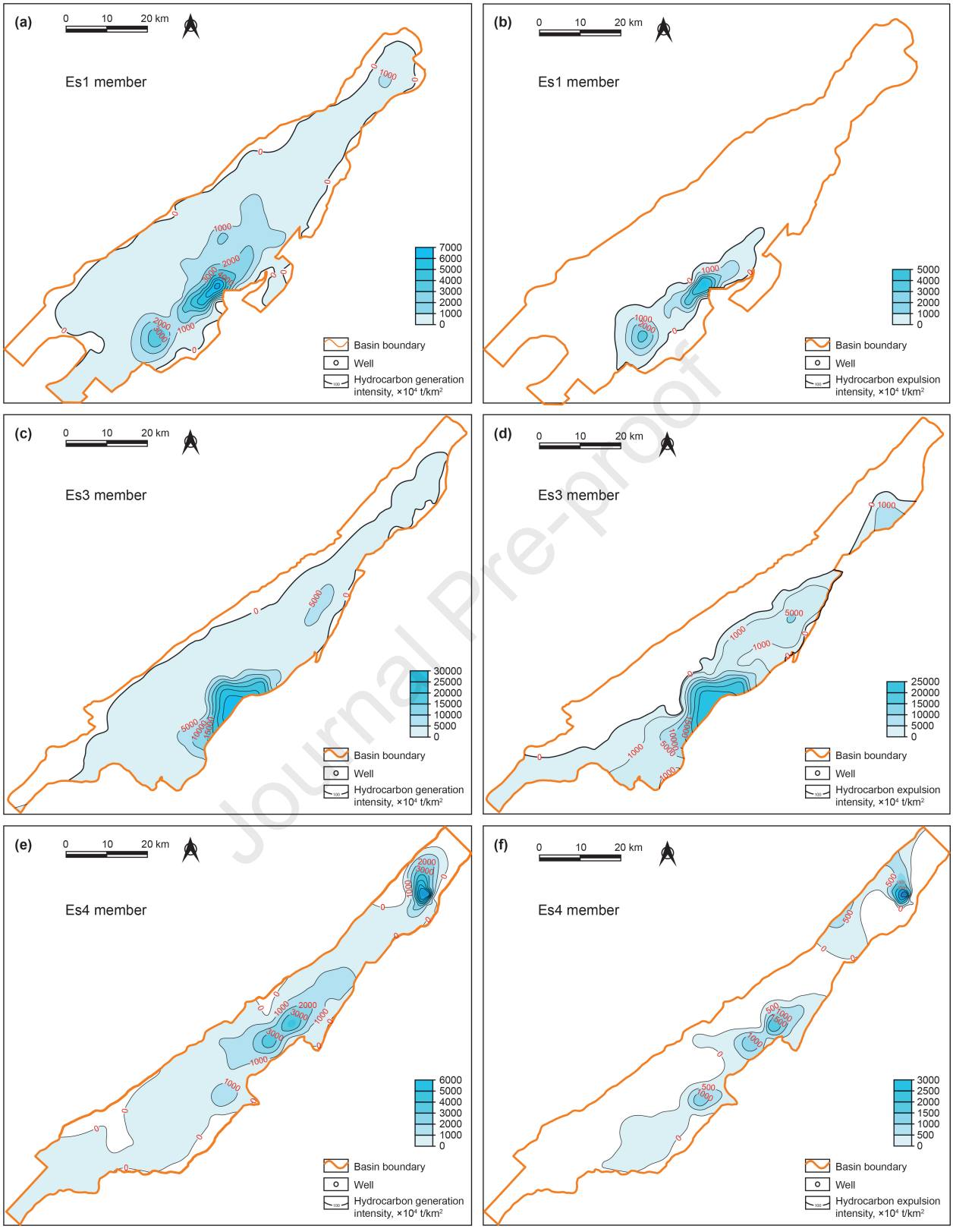

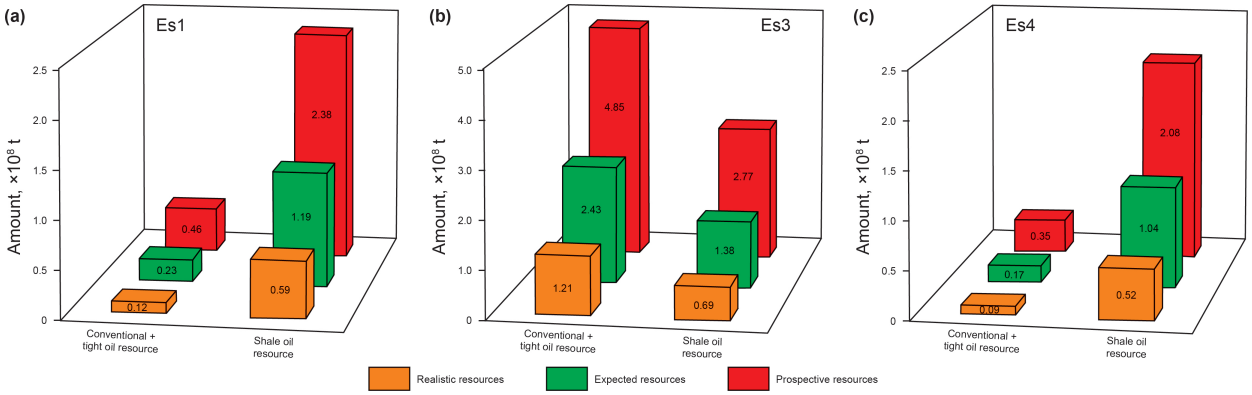

Declaration of interests

☒ The authors declare that they have no known competing financial interests or personal relationships that could have appeared to influence the work reported in this paper.

☐ The authors declare the following financial interests/personal relationships which may be considered as potential competing interests: